FACULDADE DE ENGENHARIA DA UNIVERSIDADE DO PORTO

Performance Assessment of the DLPA in Radio Frequency Identification

Erick Lima

VERSÃO DE TRABALHO

VERSÃO DE TRABALHO

Supervisor: Prof. Dr. Henrique Manuel de Castro Faria Salgado

Co-Supervisor: Dr. Mário Rui Silveira Pereira

January 28, 2017

Performance Assessment of the DLPA in Radio Frequency Identification

Erick Lima

VERSÃO DE TRABALHO

January 28, 2017

Abstract

Nowadays, to be competitive is a growing challenge, and in this sense, Radio Frequency Identification (RFID) takes an essential role. This technology consists in Automatic Identification of objects, people, animals, and others applications, always seeking for time reduction and efficiency, which are mandatory requirements in a competitive world.

The RFID technology has been replacing the well knowns barcodes, due to its capacity to improve the distance range and to avoid physical contact between the tag and the reader. Due to these particular characteristics, in the last years, researchers have been working in this technology trying to improve it and to increase the memory capability.

In this work, a novel encoding and decoding system was investigated, i.e, a novel tag, based on the Discreet Layer Peeling Algorithm (DLPA). Therefore, the main goal was the performance characterization of the algorithm in a practical scenario. This process consists in encoding of information in a Discrete Transmission Line (DTL), in which, each section correspond to a unique bit pattern. Later, the impedance sections are recovered using the DLPA from the reflection spectrum of the Transmission Line (TL). The proposed tag encode data in phase and magnitude, i.e, each pair of magnitude and phase correspond to a unique bit pattern.

This work started with an in-depth study of the DLPA and its implementation in Matlab. Next, the electromagnetic simulator Advanced Design System (ADS) was used to study several combinations of Transmission Line (TL) sections, in order to evaluate an efficient impedance encoding and to get some insight about practical limitations using momentum simulation, that takes into account several aspects, as for example, Radiation Loss and Substrate Loss. Yet, the study of Ultra Wide Band (UWB) antennas, which is an important part of an RFID system, was carried out in the specialized electromagnetic simulator FEKO.

For experimental evaluation, two tags it were manufactured in Microstrip technology and UWB antennas were used. Next, an experimental setup was carried out, in which a VNA (Vector Network Analyser), a commercial horn antenna, a UWB antenna manufactured under the scope of this work and RF cables to connect the VNA to the reader antenna, were used. Thus, the tag reflection spectrum was accessed successfully without physical contact between the reader and the tag. Lastly, the reflection spectrum was processed and, the impedances were recovered using the DLP algorithm.Thus, the functionality of the DLP in a practical scenario and a novel tag system was successfully demonstrated.

Index Terms – Discreet Layer Peeling; RFID chipless tag, Ultra Wide Band; Radio Frequency Identification; Inverse Scattering; Radio Frequency Identification chipless tag; Discreet Transmission Line; Coplanar Wave-Guide; Microstrip Transmission Line.

Resumo

No mundo moderno, ser competitivo é cada vez mais exigente e, neste aspeto, Radio Frequency Identification (RFID) assume um papel importante. Esta tecnologia consiste na Identificação Automática de objetos, pessoas, animais, entre outras aplicações, visando responder às necessidades de mercado de forma rápida e eficiente e, desta forma, fazer face à concorrência

A tecnologia RFID tem vindo a substituir os tradicionais códigos de barra, pela sua capacidade de operar a distâncias maiores e sem a necessidade de haver contacto físico. Devido a este importante diferencial, nos últimos anos, têm surgido várias publicações científicas em torno desta tecnologia, visando o seu aperfeiçoamento e a procura cada vez mais de se garantir maiores capacidades de armazenamento de informação.

Neste trabalho, investigou-se uma nova forma de codificação e descodificação de informação, ou seja, uma nova tag, baseada no algoritmo Discrete Layer-Peeling (DLP) . Assim, o principal objetivo foi o estudo da viabilidade do algoritmo num cenário real. Este processo consiste na codificação de informação numa linha de transmissão discreta, em que, cada secção, corresponde a um conjunto de bits unicamente descodificável, para posterior utilização do DLP para se tentar descobrir o valor das impedâncias através do espectro de reflexão da linha de transmissão. A tag proposta, codifica a informação em magnitude e fase, ou seja, cada par formado por magnitude e fase corresponde a um conjunto de bits único.

Desta forma, começou-se por realizar um estudo aprofundado do algoritmo DLP e sua implementação no Matlab. De seguida, utilizou-se o simulador electromagnético ADS para analisar várias combinações de linhas de transmissão por forma a encontrar a melhor forma de codificação de impedâncias e prever possíveis limitações praticas através de simulação pelo método dos momentos, isto porque, tem em consideração diferentes aspetos, como por exemplo, perdas por radiação e no subtrato. Ainda, em ambiente de simulação, foi realizado o estudo de antenas Ultra Wide Band, que constituem uma parte importante de qualquer sistema RFID. Para o estudo das antenas utilizou-se o simulador especializado FEKO.

Para a validação experimental, foram construídas tags em tecnologia Microstrip e antenas UWB. Após a construção desses dispositivos, desenvolveu-se um *setup* experimental, na qual foi utilizado um Vector Network Analyser (VNA), uma antena comercial e uma antena UWB construída no âmbito deste trabalho. Desta forma, conseguiu-se obter o espectro da tag sem que esta estivesse ligada diretamente por cabo RF ao VNA. De seguida, procedeu-se ao processamento dessa informação e da sua descodificação, verificando-se assim, a funcionalidade do algoritmo em cenários práticos e ruidosos.

Palavras Chave– *Discreet Layer peeling; RFID chipless tag, Ultra Wide Band; monopole antennas; Radio Frequency IDentification; Inverse Scattering; Radio frequency identification, chipless tag; Discreet transmission line; Microstrip transmission line.*

Agradecimentos

Para chegar até aqui, já contei com o apoio de muita gente. Gostaria então de endereçar os meus agradecimentos da seguinte forma:

Gostaria de em primeiro lugar, agradecer ao meu orientador, Prof. Dr. Henrique Manuel de Castro Faria Salgado, pelas cadeiras de especialização que tive o privilégio de ter com ele e pelo imenso conhecimento e profissionalismo que sempre demonstrou.

Em segundo lugar, gostaria de agradecer ao meu coorientador, Dr. Mário Rui Silveira Pereira, pela prontidão e pelo seu vasto conhecimento que sempre atendeu e ajudou a resolver as minhas questões durante a realização deste trabalho. Agradecer também, a enorme qualidade do trabalho previamente realizado, pelo qual eu me guio.

Ao Dr. Luís Manuel Pessoa, pelas ideias e discussões fortuitas durante os períodos de realização das reuniões, bem como, pela revisão deste documento, suporte e assistência técnica prestada.

À minha mãe, Júlia Delgado, cujo apoio e dedicação não tenho palavras para descrever. À minha irmã e amiga, Elanice Lima, pelo incansável apoio ao longo de toda a minha vida e, em especial no decorrer desta etapa. À minha Caroncha, Bruna Cristina, pelo apoio, dedicação, preocupação e presença constante na minha vida. Sem estas três, teria sido certamente muito mais difícil e sem brilho. A toda a minha família que, mesmo distantes não param de me apoiar.

Aos meus colegas e amigos, Bruno Gonçalves, Éder Oliveira, Hugo Santos, Oluyomi Aboderin, Patrício Lima, Ricardo Pereira, Joana Tavares e Wilson Silva pelas presenças e apoio nos estudos, na realização deste trabalho e nos cafés.

A todos os meus colegas e amigos de especialização, Diogo Lage, Paulo Silva, Pedro Teixeira, Rui Azevedo e Rui Gomes.

À equida de vigilância do INESC-TEC pelo excelente trabalho e sem nunca perder a simpatia mesmo em horários estranhos.

A todos vocês que passam pela minha cabeça neste momento. É impossível enumerar todos, mas certamente vocês não são menos importantes.

A todos aqueles que sempre me acompanharam e que vão me continuar a acompanhar e os que vão aparecer e que certamente terão um papel importante na concretização dos meus objetivos.

Erick Lima

"Ninguém é tão grande que não possa aprender e, nem tão pequeno que não possa ensinar."

Esoto

Contents

List of Figures

List of Tables

Abbreviations and Symbols

ADS	Advance Design System
AIS	Automatic Identification System
CMT	Couple Mode Theory
CNTT	Continues Nonuniform Transmission Line
CTL	Continues Transmission Line
DLP	Discrete Layer-Peeling
DLPA	Discrete Layer Peeling Algorithm
DNTL	Discrete Nonuniform Transmission Line
DSP	Digital Signal Processing
DTL	Discrete Transmission Line
GLM	Gel'fand-Levitation-Marchenko
IS	Inverse Scattering
MoM	Method of Moments
MTL	Microstrip Transmission Line
PEC	Perfect Electric Conductor
PLF	Power Loss Factor
RFID	Radio Frequency Identification
SOLT	Short Open Load
TEM	Transverse Electro Magnetic
TL	Transmission Line
UHF	Ultra Hight Frequency
UWB	Ultra Wide Band
VCO	Voltage Controller Oscillator
VNA	Vector Network Analyser

c	Light speed
d	Dielectric hight
E	Electric field intensity
f	Frequency
F_c	Central frequency
H	Magnetic field intensity
K	Coupling coefficients
l_{phy}	Physical length
t	Conductor thickness
T	Period
W	Microstrip line width
Z_i	Impedance section i

ω	Angular frequency
Γ	Reflection coefficient
ε_e	Effective dielectric permittivity
ε_r	Relative dielectric permittivity
μ_0	Free space permeability
β	Phase Constant
γ	Propagation constant
α	Attenuation constant
ϕ	Electric length
μ_0	Free space permeability
ε_0	Free space permittivity
$\Re$	Real part
$\Im$	Imaginary part

Chapter 1

Introduction

This Chapter presents a brief introduction to RFID technology and its importance in the modern world as well as the main goals and the context of the present work. Additionally, a brief description of the structure of this document is presented.

1.1 Thesis Presentation

This work is aligned with a topic previouly explored within a PhD thesis carried out at INESC TEC[18]. It was proposed by my supervisor, Prof. Dr. Henrique Manuel de Castro Faria Salgado and my Co-Supervisor, Dr. Mario Rui Silveira Pereira. The submission of this work to jury evaluation is intended to allow for the obtention of the master degree in Telecommunications. The work was developed at INESC TEC in cooperation with Faculdade de Engenharia da Universidade do Porto (FEUP).

1.2 Motivation

Radio Frequency Identification (RFID) is one of the many identification techniques used for assisting machines to identify people or objects automatically. Many RFID applications exist with different purposes: commerce, logistical distribution, material distribution, large scale production, to name a few. This technology has the purpose to improve industrial processes seeking for resource expenditure reduction and process optimization, thus rendering more competitive products, both in price and quality.

In addition to RFID, several Automatic Identification Systems (AIS) exist, which include: smart cards, barcodes, voice recognition, biometric technologies, to name a few. Between them, perhaps, the best known are the traditional barcodes, which present some limitations such as short range applications and low memory capability [8]. In order to overcome such limitations, in the last years, RFID systems have been investigated. RFID systems allow for automated tracking, increase of the read range, as well as full operationality without physical contact between the reader and the tag.

However, the first generation of RFID systems were based on active chips, which provide longer range, while requiring a battery, and passive chips, which work in short range, without battery. However, the cost associated with the integrated circuit led to the emergence of a second generation of RFID systems, known as chipless RFID systems.

In this work, a novel chipless RFID system with improved storage capacity was investigated. The main idea is to recover an encoded impedance profile, which constitutes the proposed tag, based on the Discreet Layer Peeling Algorithm. Thus, first it is necessary to encode the impedances. After the codification, the impedances are recovered with the Discreet Layer-Peeling algorithm, in which the input data is obtained from the reflection spectrum of the tag.

1.3 Objectives

The main objectives of this work are the following:

- Implement and test the DLP algorithm.
- Investigate feasible impedance encoding techniques.
- Design, fabricate and characterise UWB antennas.
- Implementation of selected tags and experimental evaluation of system performance.

In achieving these objectives we will be able to advance the state of the art in this area of chipless RFID tags, by showing a novel technique based on the encoding of information on the impedance of a transmission line.

1.4 Problem characterization

Given the general objectives presented in Section 1.3 our specific aim is:

- Implementation and testing of the DLPA. The algorithm will be implemented in Matlab, taking advantage of the software built-in tools. The input data of the DLPA is the reflection spectrum, S_{11}, of a tag, provided, in first instance, by the software ADS, in which the tags will be designed and simulated. The final test of the DLPA will be made, using as input data, the reflection spectrum of experimentally measured tags, printed in substrate Rogers Duroid RO4003C. The reflection spectrum of the tag will be obtained using a VNA.
- Several impedance encoding techniques will be investigated in order to improve the memory capacity and tag dimensions. To achieve these goals, the maximum number of different impedances that can be encoded and recovered with accuracy under noise environment will be investigated.

- Ultra Wide Band (UWB) antennas will be designed and simulated using the 3D electromagnetic simulation software FEKO from Altair. UWB antennas are needed due to the fact that we need to interrogate the tags along a large frequency range (in our case a range of 2.5 GHz), in order to obtain a half period of the reflection spectrum. The tags that will be designed are similar to a discrete system, therefore, characterized by the spectrum periodicity. Thus, it is possible to reconstruct the system knowing only one period of the spectrum.

1.5 Contributions

- Experimental evaluation of the DLP algorithm to recover impedance sections of a Discrete Transmission Line (DTL) was demonstrated by the first time.
- A new chipless tag, including the antenna section, based in the DLP was successfully demonstrated.

1.6 Outline

This document is organized in six Chapters. Each chapter starts with a small introductory text describing the chapter content and with the exception of the present one, ends with a brief summary.

The present chapter introduces the motivation behind chipless RFID systems and the main objectives of this work. Chapter 2, starts with the relevant Transmission Line concepts relevant in this work. After this section, the *state-of-the-art* in RFID systems is presented. Additionally, Section 2.1 presents the DLP theoretical foundations and its *state-of-the-art*.

In Chapter 3, the proposed system design is discussed and simulation results of the DLP implementation are presented including a validation of its performance under noise, using data provided from the electromagnetic simulator ADS. Also, some practical limitations are discussed.

Chapter 4 presents the experimental procedure and the tools that were used as well as the experimental results obtained in this work. The results, include the UWB antenna radiation pattern, the tag's reflection spectrum, and the performance of the DLP algorithm. The performance characterization of DLP includes the recovering of the independence sections and the error obtained in each section. Finally Chapter 5 provides the conclusions of this work as well as possible avenues for future work.

Chapter 2

State-of-the-art

This Chapter starts with some important Transmission Line concepts related with this work, in which the differences between continuous and Discrete Transmission Lines (DTL) are presented as well as some useful equations. Subsequently, the RFID history, as well as its *state-of-the-art* and the most important blocks are presented. Lastly, the Discrete Layer-Peeling Algorithm, which is a central topic of this work, and its theoretical principles are discussed.

2.1 Transmission Line concepts

2.1.1 Continuous Transmission Line

A Continuous Transmission Line is one for which the electrical parameters do not change abruptly, resulting in a smooth impedance profile, as illustrated in Figure 2.1. The behaviour of these type of structures can be easily accessed using an electromagnetic simulator *software* like FEKO, ADS or HFSS. However, analytical study of a continuous non-uniform Transmission Line is quite complex and gives rise to tedious equations that are out of the scope of this work. Mathematical derivations of the most important parameters, for example, the reflection and transmission coefficients, based in coupled mode theory can be found in [4].

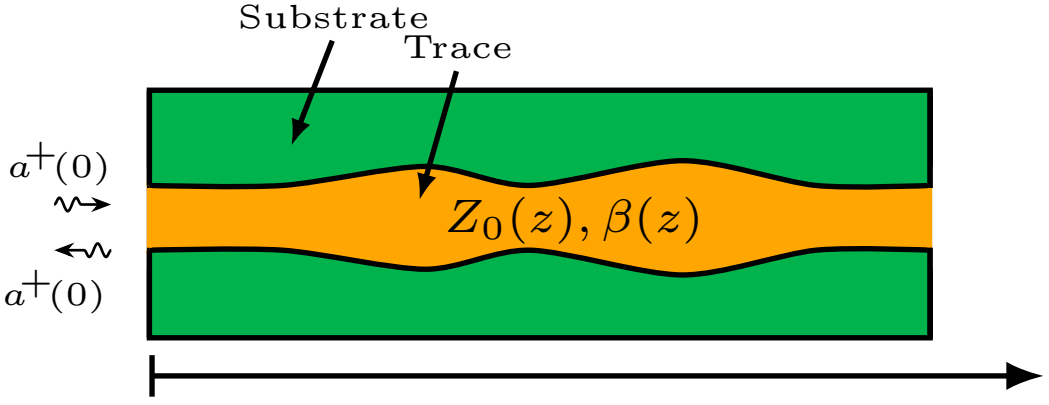

Figure 2.1: Continuous transmission line profile

2.1.2 Discrete Transmission Line Theory

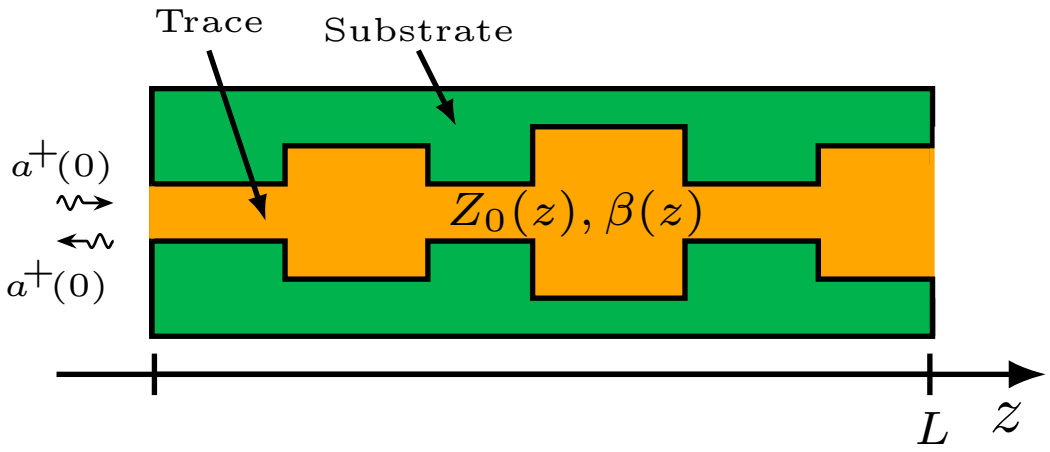

Figure 2.2: Discrete Transmission Line profile

On the other hand, a Discrete Transmission Line (DTL), can be considered as a particular case of a Continuous non-uniform Transmission Line (TL), in which, the impedance is constant along each section, as illustrated in Figure 2.2. An alternative illustration of an DTL is depicted in Figure 2.3, as a cascade of *Networks*, each one representing a TL section. The symbols, a^+ and a^-, represent the forward and backward propagation, respectively. In each section, part of the forward signal is coupled to the backward signal and part of the backward is coupled to the forward, resulting on an infinite reflection phenomenon inside of the TL. This phenomena, will be better explained in Section 2.3.

In this particular case, it is convenient to perform the mathematical explanation using the T-parameters, which describe each section by means of the T-matrix [20, 17].

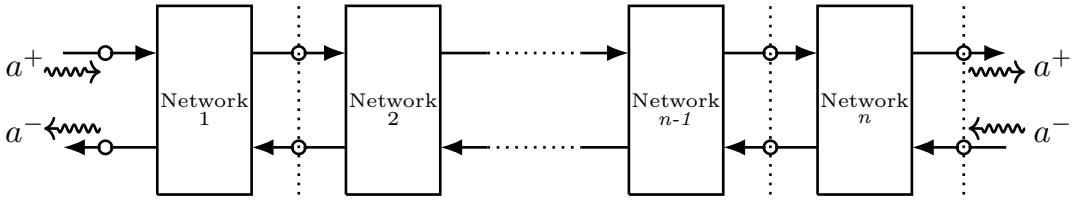

Figure 2.3: Cascade connection of n 2-port networks.

A single section of a two port device is described by the equation (2.1)

$$\begin{bmatrix} b_{i+1}^+ \\ b_{i+1}^- \end{bmatrix} = \begin{bmatrix} T_{i,i} & T_{i,i+1} \\ T_{i+1,i} & T_{i+1,i+1} \end{bmatrix} \begin{bmatrix} a_i^+ \\ a_i^- \end{bmatrix} \tag{2.1}$$

in which, a_i^+ and a_i^-, represent the forward and backward signal, respectively, at the input port of the Network $_i$, b_i^+ and b_i^- represent the forward and backward signal at the output port of the Network$_{i+1}$ and $T_{i;i}$; $T_{i;i+1}$; $T_{i+1;i}$; $T_{i+1;i+1}$ are the transmission coefficients between ports. According to the illustration in Figure 2.4, Equation (2.1), becomes as [17]:

$$\begin{bmatrix} a^+(\omega,x_i) \\ a^-(\omega,x_i) \end{bmatrix} = \frac{1}{\sqrt{1-\Gamma_i^2}} \begin{bmatrix} e^{j\omega\Delta l} & \Gamma_i e^{-j\omega\Delta l} \\ \Gamma_i e^{j\omega\Delta l} & e^{-j\omega\Delta l} \end{bmatrix} \begin{bmatrix} a^+(\omega,x_i+\Delta l) \\ a^-(\omega,x_i+\Delta l) \end{bmatrix}$$

where Γ_i is the reflection coefficient at the two section interface given by:

$$\Gamma_i = \frac{Z_{i+1} - Z_i}{Z_{i+1} + Z_i} \tag{2.2}$$

Δl is the physical length, ω is the angular frequency, and Z_i is the impedance at the interface of each section. The T-matrix that describes the complete device is given by the product of the elementary T-matrix of each section, mathematically described as:

$$T = T_1 T_2 T_3 ... T_n \tag{2.3}$$

Relating the S-parameters and T-parameters, from equation (2.3), it is possible to write that [20]:

$$S_{11} = \frac{T_{12}}{T_{22}} \tag{2.4}$$

$$S_{12} = \frac{T_{11}T_{22} - T_{12}T_{21}}{T_{22}} \tag{2.5}$$

$$S_{21} = \frac{1}{T_{22}} \tag{2.6}$$

$$S_{22} = \frac{1}{T_{21}} \tag{2.7}$$

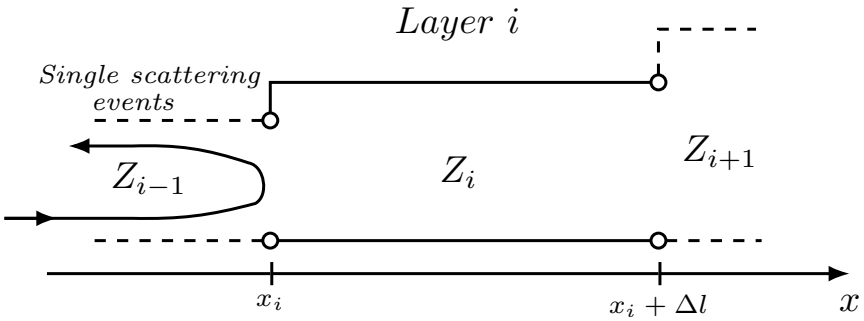

Figure 2.4: Constant impedance layer. The coupling energy between the forward and back-word propagation modes is an instantaneous and localized event that takes place at depth x_i

In order to better understand the properties of a DTL, Equations (2.4) to (2.7) were implemented in Matlab. Results of the reflections spectrum, S_{11}, of the circuit depicted in Figure 2.5, was obtained for different values of the central frequency, F_c. It was considered three different values, equal to 5, 10 and 15 GHz. Figure 2.6, illustrate the obtained results and it is possible to conclude that a DTL is periodic, with periodicity equal to the designed central frequency, F_c. Also, it is possible to relate a DTL with Digital Signal Processing (DSP), comparing Figure 2.6 and Figure 2.7, in which, the continuous signal, $h(t)$, is the analogue of a Continues Transmission Line (CTL) and the Digital signal, $r[n]$, is the analogue to a Discrete Transmission Line in terms of the frequency spectrum.

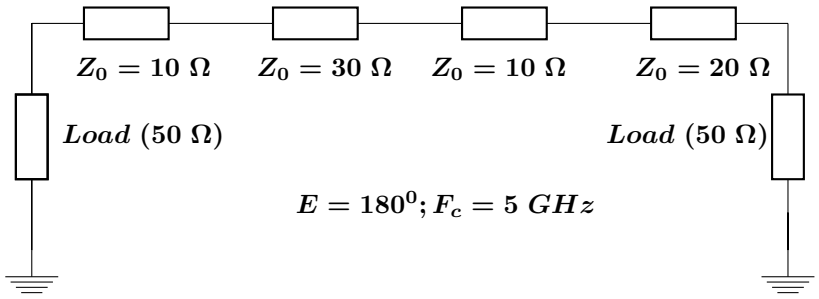

Figure 2.5: Discrete Transmission Line terminated at 50 Ω *Load* used to validate the implementation of the Equations (2.4) to (2.7).

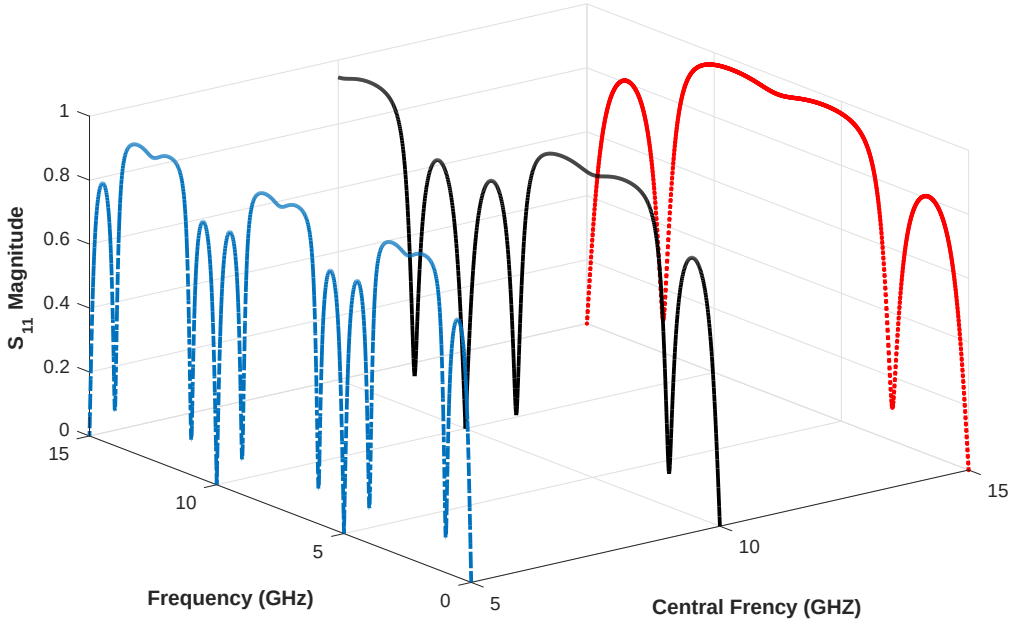

Figure 2.6: Reflection spectrum, S_{11}, of the Discrete Transmission Line depicted in Figure 2.5.

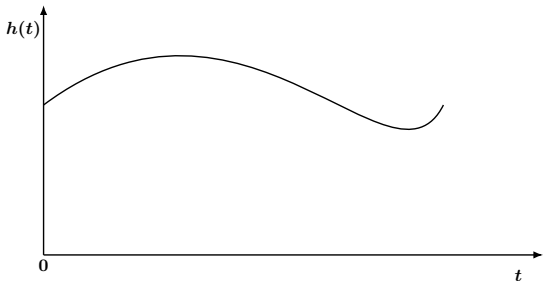

(a) Analog domain. Continuous-time impulse

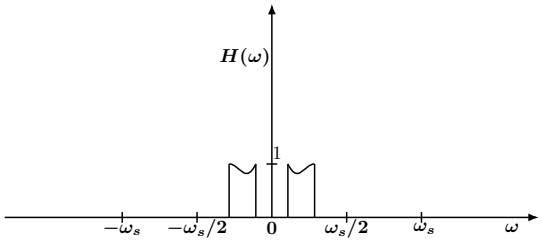

(b) Continuous time Fourier transform of $h(t)$.

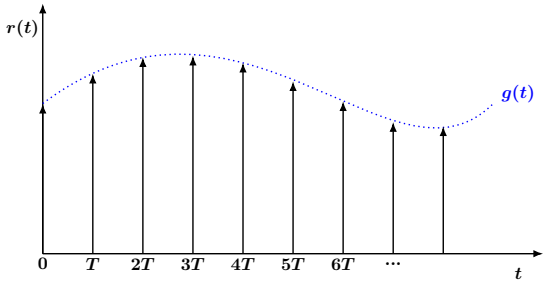

(c) Periodic sample impulse response with period T.

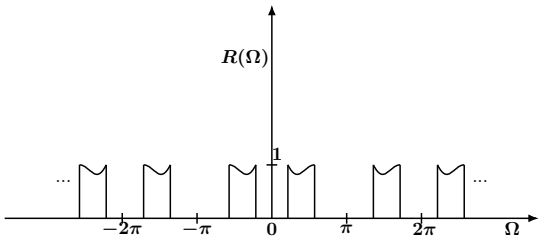

(d) Continuous time Fourier transform of $r(t)$.

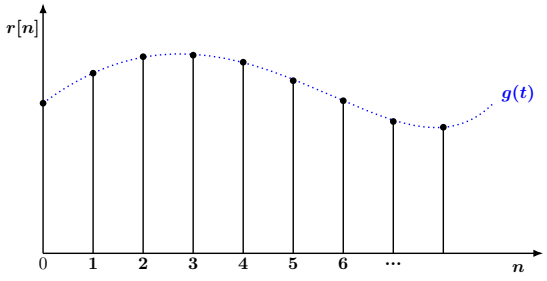

(e) Digital Domain. Discrete-time impulse response

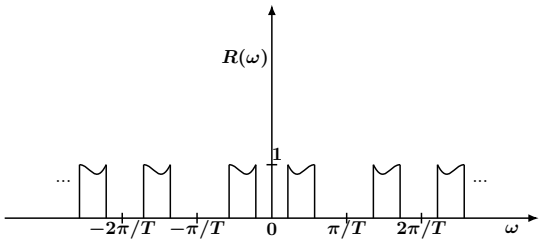

(f) Discrete-time Fourier transform of $r(n)$

Figure 2.7: Relationship between analog domain and digital domain.

2.2 Radio Frequency Identification

In this section, a brief RFID history is exposed. Also, a typical RFID architecture and all of its main components are presented.

2.2.1 RFID History

The RFID technology was first used by means of radar equipment improvement, to recognize and distinguish between the enemy and friend military aircraft in World War II (1940) by the British Royal Air Force [1]. In 1948, a revolutionary paper entitled *Communication by means of reflected power* was reported. Unlike the conventional radar system, in which the reflected signal dictates whether the target is present or not[1], in this concept, the target is capable of modulating the transmitted signal and then reflected it back to the transmitter with added information. In this way, all targets can be made to modulate the signal with their own characteristics [28]. This invention of passive communication created a new dimension in the RFID sector and led the other researchers to explore the RFID technology in a broader scenario. In 1960, a pioneer paper on passive RFID, entitled *Radio transmission systems with modulatable passive responder* was reported [3]. On the early 1970's, multi-bit functional passive UHF RFID systems with a range of several meters have been introduced for the first time. Due to improvements in radios and integrated circuits, RFID has undergone through an incredible progression. As a result RFID got high attention from retailing organizations and governments. In the following decades, various experiments of RFID have been reported. In 2010, a paper entitled *Multiresonator based chipless RFID tag and dedi-cated RFID reader*[23] was reported. In this paper, the carrier signal is modulated both in phase and magnitude leading to a significant memory capacity improvement. In the present work, we propose a new tag also capable to modulate the carrier in phase and magnitude, but the decoding information will be made by the DLP algorithm for the first time.

The most relevant publications in the last years, are summarized in the next table.

[1] This can be interpreted as a on-off modulation

Ref.	Yer	Title	Characteristics
[26]	2009	A chipless rfid sensor system for cyber centric monitoring applications.	AM [a]. 16-bit system.
[21]	2009	Multiresonator-based chipless rfid system for low-cost item tracking	AM and PM[b]. 35-bit system.
[22]	2009	Design of fully printable planar chipless rfid transponderwith 35-bit data capacity.	Spectral signature[c].35-bit system
[23]	2010	Multiresonator based chipless rfid tag and dedicated rfid reader.	Spectral signature. CPW[d]. 20-bit system
[30]	2011	Chipless rfid tag using hybrid coding technique.	Reduced dimension. 30-bit system
[32]	2012	High-capacity chipless rfid tag insensitive to the polarization.	Insensitive to polarization[e]. 19-bit system
[31]	2012	A fully printable chipless rfid tag with detuning correctiontechnique.	Single layer[f]. ASK modululation. 20-bit
[14]	2015	Spectral extraction of chipless RFID tag using time domain analysis.	SIR[h].10-bit system
[35]	212	Novel chiplesstag with electromagnetic code.	spectral signature. smaller size. 10-bit
[7]	2015	Angle-based chipless rfid tagwith high capacity and insensitivity to polarization.	Polarization-independent. three-bit per element.
[34]	2014	Dual-polarizedchipless rfid tag with temperature sensing capability.	Monitoring temperature capability.
[24]	2011	Rfid system based on fully printable chiplesstag for paper-/plastic-ltem tagging.	CPW. Low cost. 23-bit system
[16]	2013	Low cost chipless tag with multi-bit encoding technique.	Stepped impedance resonator.
[15]	2015	Design of a chipless rfid tag using cascaded and parallel spiral resonators at 30 Ghz.	shorte range application. 6-bit prototype

[a]Amplitude Modulation ,i.e., the amplitude of the backscattered data is changed. [b] Phase modulation. [c]Both amplitude and phase components of the spectral signature are used for data encoding. [d]Low cost configuration. [e]Making the design of the reader easier since only linear polarization is needed to detect the tag. [f]Its fabrication process is potentially very cheap because it needs only one conductive layer, so that it can be fully printed directly on the product. [h]Stepped Impedance Resonator.

2.2.2 Hardware Components

2.2.2.1 Tag

Tags[2] are the physical devices that carry the identifications of objects, animals, inventory products etc. A distinction is usually made between passive and active tags. Also, memory capacity and read-write capability are useful distinguishing factors [29].

Passive Tag

Passive tags do not have an internal source of power and cannot send outbound signals without receiving energy from a reader. After receiving an incoming RF signal, the integrated circuit receives power and transmits an outbound signal. Passive tag antennas must be able to receive the incoming radiated power and radiate the outbound signal. Also, their life time is almost unlimited.

Another important fact is that nowadays it is not mandatory that passive tags contain a silicon chip. In fact, researchers have already proposed chipless RFID tags. Chipless tags eliminate the cost associated with the manufacture of the integrated circuits while providing a better life time. The system proposed in this dissertation is included in this category.

Active Tag

Unlike passive tags, active tags have their own energy sources, having therefore the capability to generate an outbound signal. Active RFID tags can be programmed to broadcast their own signals at certain time or when external events occur to form an active RFID system. This type of tag is usually powered by a local battery to provide a much longer reading range compared to passive tags. However, these tags are typically used in environments with high mobility requirements and they are much more expensive. Also, the active tags life time is mainly dependent on the battery. When the battery fails, the active tags will need to be replaced.

2.2.2.2 RFID Reader

A diagram of the RFID reader is represented in Figure 2.8. The RFID reader sends out an electromagnetic wave that hits the passive RFID tag which scatters back a wave with the information encoded in the backscattered signal. The tags proposed within this dissertation modulate the interrogated signal both in phase and magnitude, thus improving memory capacity. Active RFID tags do not require the power from the reader to be activated. At the present time, RFID readers typically consist of:

[2] also called transponders or target

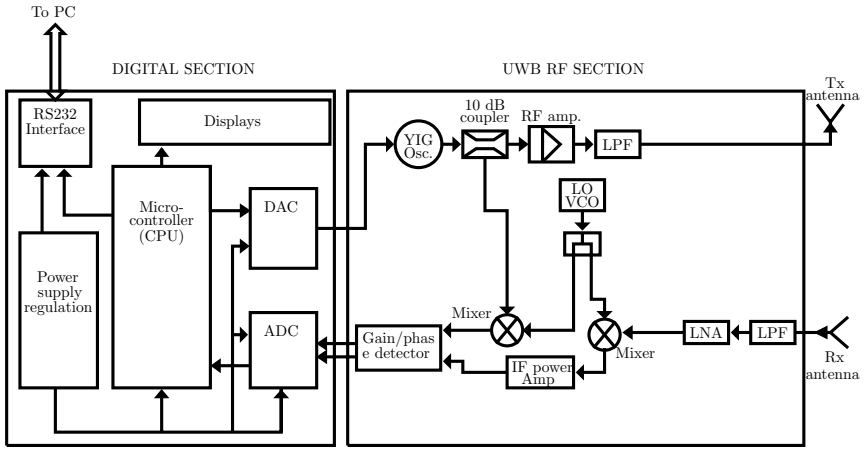

Figure 2.8: Block diagram of an RFID reader for chipless tag reading. [23]

1. One or more antennae,
2. A signal processing unit (typically digital domain),
3. Software application,
4. Additional electronics.

For the purpose of operation of the tag proposed in the present work, the type of antenna considered is Ultra-Wide Band (UWB) [6, 12, 19] due to the fact that the short pulse used to interrogate the tags require a large bandwidth. Also, the antenna should be omnidirectional along the entire frequency range. Although in practice this is not entirely feasible due to the radiation pattern distortion.

The RFID reader usually is provided with two antennas. One of them is responsible for the inbound signal and the other for the outbound signal. The antennas must be cross-polarized in order to provide better isolation between the interrogation and the received signal. On the other hand, it is possible to use just one antenna for transmission and reception, but in this particular case the receiver has to be provided with a means of separation of the transmitted and received signal, such as a circulator. Also, the tags have to be equiped with one antenna capable of delivering the emitter radiated power to the tag as well as radiating the scattered power from the tag.

A Mixer is used to convert the RF signal to an intermediate frequency (IF) signal, followed by a phase detector. In a simple way, the mixer can be understood as a mathematical operation in which the received signal is multiplied by a sinusoid or square wave with a properly designed frequency. The modulator signal is generated by the voltage controlled oscillator (VCO). In the frequency domain the mixer operation converts the signal to a different band, either the sum or difference of the original input frequencies. Additionally, it is necessary to use an IF filter to remove the upper or lower band.

The signal received from the tag and the reference signal are compared in amplitude and phase by the phase detector. The amplitude and phase difference are given as separate DC values by the

phase detector. The 2 DC values are multiplexed and then sent to the digital section where they are digitized and further processed on for tag ID detection.

The interrogation signal is generated at a YIG oscillator installed in the RF section. Unlike conventional oscillators that operate in a very narrow band, the YIG oscillator is capable of sweeping the frequency up to 6 GHz. Finally the interrogation signal is amplified, filtered and lastly delivered to the antenna. Finally, at the core of digital section is a micro-controller where all digital processing of data is performed.

Due to the limited time available to carry out the present work, the entire digital section functionality will be performed offline in a personal computer running Matlab, while the reader hardware will be based on a laboratory VNA.

2.3 Discrete Layer Peeling

This section presents an historical review of Inverse Scattering theory and its applications. Also, a theoretical introduction to the DLP algorithm is presented, which is one of the methods used to obtain an Inverse Scattering solution.

2.3.1 Inverse Scattering From an Historical Perspective

Inverse scattering (IS) allows one to reconstruct the physical properties of an unknown system from the scattered[3] data. In the specific case of this work, IS will be used to reconstruct the impedance profile of a transmission line used to encode information. In order to perform this, one must probe the target with a proper signal and measure the scattered data, which corresponds to the input data to the Inverse Scattering equations. In this way, it is possible to obtain detailed knowledge of the mentioned unknown system.

Inverse Scattering was originally studied and applied by physicists and mathematicians. However, with the advances of technology, nowadays it finds applications in several areas, such as, microwave imaging, speech research, identification of the acoustic impedance or conductivity profiles in layered-earth models, the design of digital filters, underwater sound propagation, synthesis of fiber bragg gratings, and recently synthesis of microwave structures.

In the general case, considering a 3D object, as illustrated in the Figure 2.9, reflected waves occur in all directions. This gives rise to complex mathematical models due to the complex nature of the wave equations, which constitutes a complex problem. Another limitation is related with the fact that in almost every case, electromagnetic theory gives solutions only for the direct problem, i.e., the waves behavior can be known from the knowledge of the physical property with which they interact. However, for simplicity, we are only interested in one-directional propagation as illustrated at Figure 2.10. In such situations, the traveling waves are confined in a waveguide, thus minimizing the initial problem. For this particular case, the IS problem is reduced to the Gelfan-Levitation-Marchenko (GLM) Eq. (2.3.1),

[3] due to the mismatch impedance

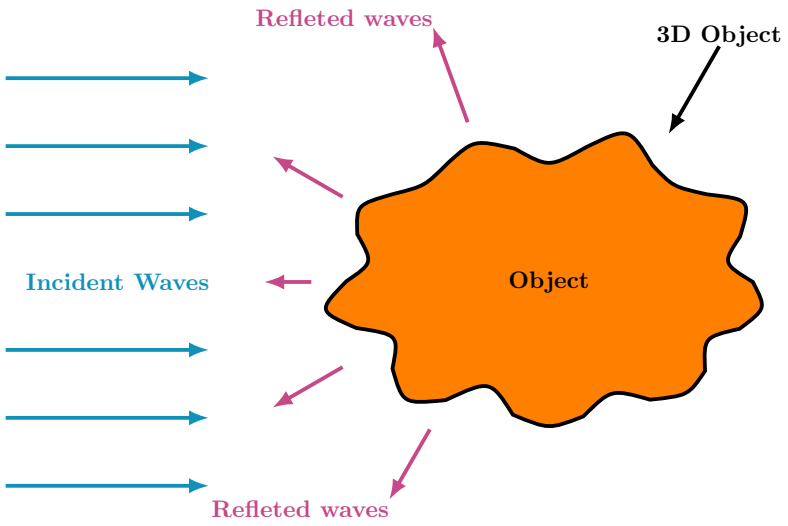

Figure 2.9: Inverse Scattering.[18]

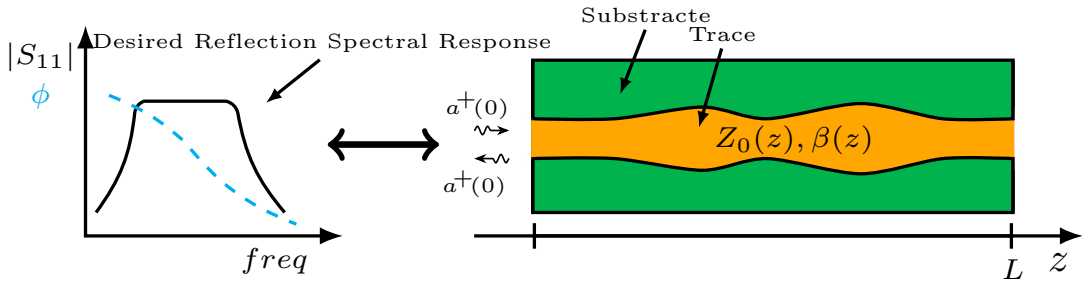

Figure 2.10: Inverse Scattering for particular case of transmission line.[18]

$$F(x+y)+K(x,y)+\int_{-y}^{x} K(x,z)F(y+z)dz=0 \tag{2.8}$$

where $F(x)$ is the Fourier transform of the reflection coefficient, given by

$$F(x)=\frac{1}{2\pi}\int_{-\infty}^{\infty} r(\omega)e^{j\omega x}dx \tag{2.9}$$

Eq. (2.3.1) appears as result of a pioneer work [11] performed by Gelfan, Levitation and Marchenko. In this way, from the GLM equation, given the reflection coefficient, $r(\omega)$, as input data and provided that there are no poles of the reflection coefficient in the right half of the s-plane (condition required for stability) it is possible to obtain the IS solution. However, GLM Eq. (2.3.1) has no analytical solution except in a few special cases. This fact has led several researchers to propose numerical methods, notably[13, 10, 9]. Based in these methods, Paul P. Roberts and Graham E.

Town have applied IS to perform the first microwave filter in 1995 [25]. By taking advantage of the fast development of electronic systems, more specifically, more powerful CPUs (Central Processing Unit) and micro-controllers, the initial numerical algorithms have been improved with the employment of fast digital signal processing (DSP). In fact, nowadays, fast processing is mandatory for any engineering development to be competitive.

So far, DLP has been mentioned as a solution for the IS problem without any reference to authors. DLP was originally published by the authors Ricardo Feced, Michalis N Zervas, and Miguel A Muriel, in 1999. The paper was entitled *efficient inverse scattering algorithm for the design of nonuniform fiber bragg gratings* and it demonstrated better results when compared to the previous methods presented in [13, 10, 9]. Later (2001), Johannes Skaar, Ligang Wang, and Turan Erdogan have taken advantages of the existing signal processing tools to improve the original DLP algorithm. Their objective was to simplify it in order to improve its clarity and efficiency, as well as employ it for the synthesis of Fiber Bragg Gratings. The results obtained are presented in [27].

Recently (2014), an exhaustive work entitled *Inverse Scattering Techniques for the Synthesis of Microwave Structures* was presented [18]. Results of DLP applied for the synthesis of *Microwave Structures* are presented in [17] by MR Pereira, HM Salgado, and JR Pereira.

Having [17] as starting point, DLP will be applied in RFID technology in this work.

2.3.2 Discrete Layer Peeling Theory

In this section, a brief theoretical introduction is presented which is necessary to understand the fundamental principles of the DLP theory.

When an electromagnetic wave interacts with a non uniform transmission line (NTL) reflection occurs at each point of the line. In this way, transmitted and reflected waves interact mutually, i.e., part of the transmitted signal is coupled back and part of the reflected signal is reflected again, causing it to be coupled forward, and this process is repeated, again and again. The coupling coefficient is given by the following Eq. (2.10):

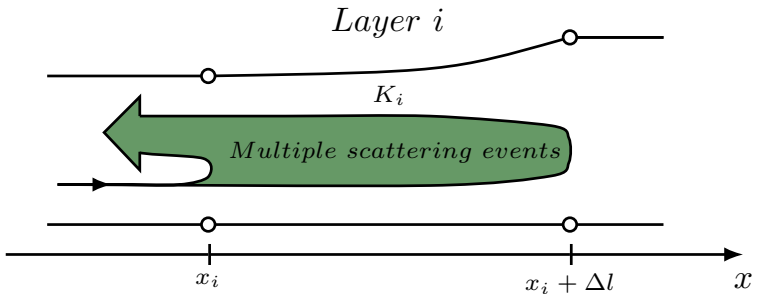

Figure 2.11: Coupling illustration. The coupling of energy between the forward and backward propagation. [18]

$$K(x) = \frac{2}{\pi} \int_{-\infty}^{\infty} R(\omega, x) d\omega \tag{2.10}$$

where $R(\omega, x)$ is the reflection spectrum at point x. If we consider that the NTL is discrete with an infinitesimally constant impedance section as illustrated in Figure 2.11, the total reflectivity of a small section Δl is given by:

$$K_{tot_i}(x) = \frac{2}{\pi} \int_{x_i}^{x_i+\Delta l} K_i(x) dx = K_i \Delta l \tag{2.11}$$

where $K_i(x) = K_i = C^{te}$ is the coupling function at section i.
Having this fact in mind, if we consider that the total coupling K_{tot_i} is concentrated in a single location and that no coupling phenomena takes place at any other location along that same layer, then assuming that the coupling occurs at the beginning of the layer, we can approximate each layer as a constant impedance transmission line (TL) of length Δl preceded by a reflector (Figure 2.12). This means that, any section of a transmission line with constant local impedance acts on the waves as a pure time-delay and time-advance operator. This behavior is translated on the following equation:

$$\begin{bmatrix} a^+(\omega, x) \\ a^-(\omega, x) \end{bmatrix} = \begin{bmatrix} e^{j\omega\Delta l} & 0 \\ 0 & e^{-j\omega\Delta l} \end{bmatrix} \begin{bmatrix} a^+(\omega, x+\Delta l) \\ a^-(\omega, x+\Delta l) \end{bmatrix} \tag{2.12}$$

A pictorial signal-graph "representation" of the waves interaction with a discrete transmission line is represented in Figure 2.13, where K_x is a none zero value (coupling factor) that represents the part of each wave being "backscattered" and added to the propagation in the opposite direction.

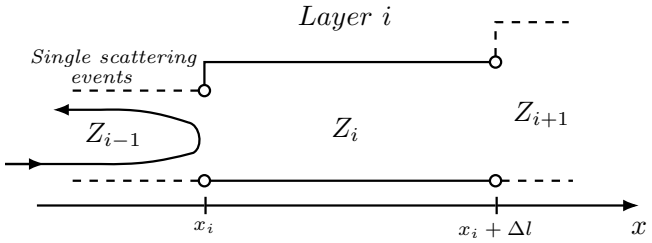

Figure 2.12: Constant impedance layer. The coupling of energy between the forward and backward propagation modes is an instantaneous and localized event that takes place at depth x_i. Z_i is the impedance of layer i and is a constant value along that layer. [18]

Eq. (2.13) describes the complete matrix transmission in a discrete layer, Δl. Unlike Eq. (2.12), the propagation coupling between the right and left waves is demonstrated. Note that Eq. (2.12) describes the waves "inside" the section while Eq. (2.13) describe the waves behavior at the

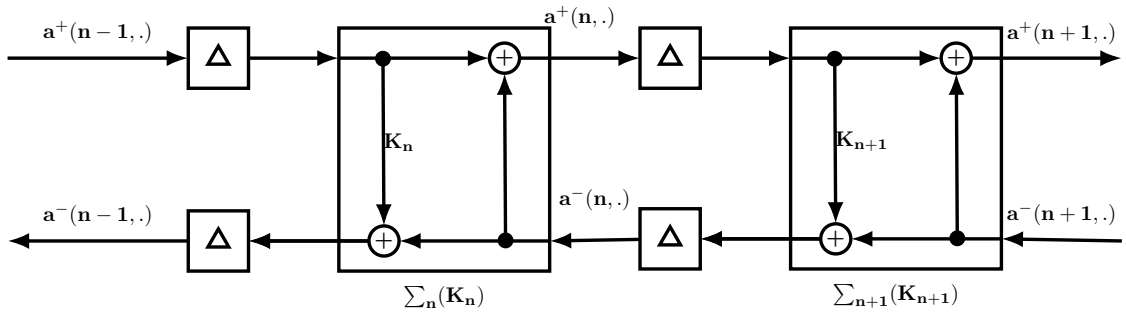

Figure 2.13: Causal scattering event signal-flow graph, where $\Delta = e^{jw\Delta l}$ and K_n is the coupling coefficient. Adapted from [5].

beginning of the section.

$$\begin{bmatrix} a^+(\omega,x) \\ a^-(\omega,x) \end{bmatrix} = \frac{1}{\sqrt{1-\Gamma_i^2}} \begin{bmatrix} e^{j\omega\Delta l} & \Gamma_i e^{-j\omega\Delta l} \\ \Gamma_i e^{j\omega\Delta l} & e^{-j\omega\Delta l} \end{bmatrix} \begin{bmatrix} a^+(\omega,x+\Delta l) \\ a^-(\omega,x+\Delta l) \end{bmatrix} \tag{2.13}$$

where,

$$\Gamma_i = \tanh(K_{tot_i}) \tag{2.14}$$

Also, note that, from the physical property of energy conservation, Γ_i is always ≤ 1. Replacing (2.14) in the transmission line impedance equation presented in [20], it is possible to obtain one important equation that gives us the impedance of a layer:

$$Z_i = \frac{1+tanh(K_{tot_i})}{1-tanh(K_{tot_i})} Z_{i-1} \tag{2.15}$$

Figure 2.14, illustrates a cascade transmission line with constant impedance section Δl. If we probe it with one impulse signal, $\delta(t)$, at some layer, the impulse response at $t = 0$ will be equal to the reflection at that layer without interference of adjacent layers. One illustration of the impulse response at $t = 0$ is set to red color in that Figure. This fact is a result of the causality property, i.e., a non-anticipate system. In this way, at t=0, it is impossible to have the contribution of the other layers, because there is not enough time for the signal to be transmitted and scattered from any other layer. So, from the Eq. 2.15, it is possible to obtain the impedance of that layer. In this way, in that layer, x_i, all the previously layers, $x_{i-1}, x_{i-2}, ...x_0$ have been identified. The scattering events triggered by $\delta(t)$ along the four sections of the structure can be visualized in the space-time diagram depicted in Figure 2.15. From the inspection of the space-time diagram and the discussion above, it is possible to conclude that the reflection impulse at the beginning of one layer, x_i, is given by the following equation:

$$\sum_{n=0}^{\infty} h_n \delta(t-nT). \tag{2.16}$$

From (2.16), it is evident that at t=0,

$$\Gamma_i = r_i(0) = h_0. \tag{2.17}$$

Knowing the reflection coefficient (Γ_i) of a layer i, and provided the coupling coefficient according to (Section 2.3.2), it is possible to obtain the characteristic impedance of each section from (Section 2.3.2). This is the main principle behind the layer peeling algorithm, which corresponds to *layer by layer identification*.

So far, we have presented the impulse response in time domain, however, it is our interest to obtain it in the frequency domain which is the input of the DLP algorithm. Considering (Section 2.3.2) in its inverse form as follows (Section 2.3.2):

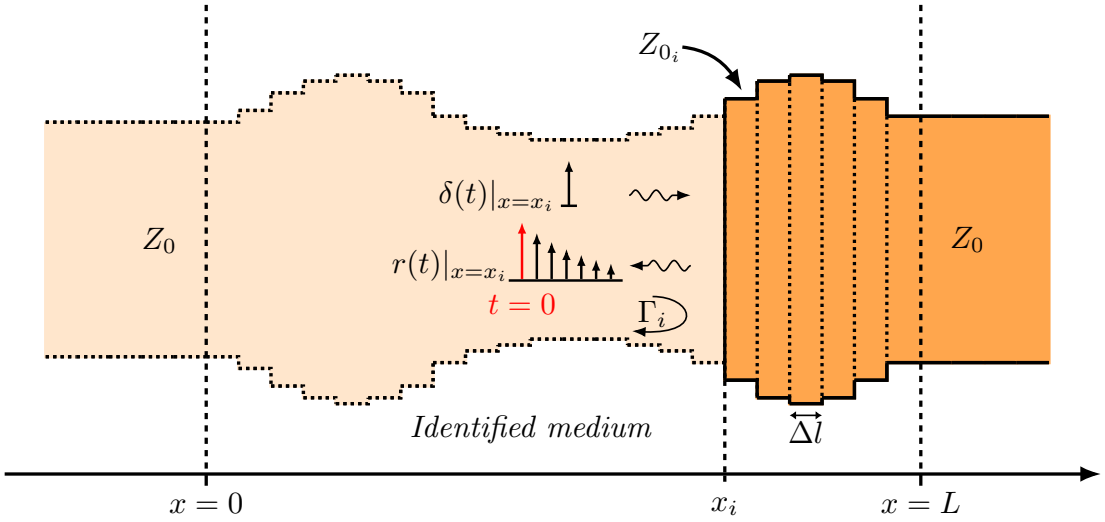

Figure 2.14: Evaluation of the local reflection coefficient Γ_i at depth x_i. The first impulse of the reflection is illustrated in red colour [18]

$$\begin{bmatrix} a^+(\omega,x_i) \\ a^-(\omega,x_i) \end{bmatrix} = \frac{1}{\sqrt{1-\Gamma_i^2}} \begin{bmatrix} e^{-j\omega\Delta l} & -\Gamma_i e^{-j\omega\Delta l} \\ -\Gamma_i e^{j\omega\Delta l} & e^{j\omega\Delta l} \end{bmatrix} \begin{bmatrix} a^+(\omega,x_{i-1}) \\ a^-(\omega,x_{i-1}) \end{bmatrix} \tag{2.18}$$

and assuming that the reflection frequency response at x_{i-1} is known, the corresponding fields amplitude can be given by,

$$\begin{bmatrix} a^+(\omega,x_i) \\ a^-(\omega,x_i) \end{bmatrix} = \begin{bmatrix} 1 \\ R(\omega)_{i-1} \end{bmatrix} \tag{2.19}$$

where $R(\omega)_{i-1}$ is the Fourier transform of the impulse response as illustrated in Figure 2.14. Replacing (2.19) into (2.18) it is possible to calculate the fields at x_i and the corresponding reflection response in the following way:

$$R_i(\omega) = \frac{a^-(\omega, x_i)}{a^+(\omega, x_i)} = \frac{R_i(\omega) - \Gamma_{i-1}}{1 - \Gamma_{i-1}} e^{j2\omega\Delta l} \tag{2.20}$$

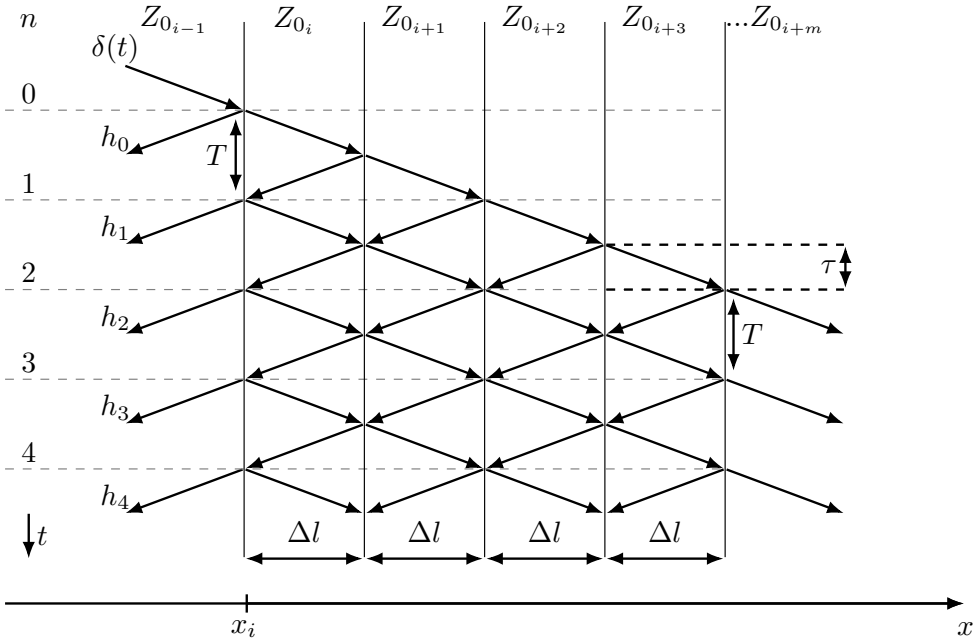

Figure 2.15: Space-time diagram of incident and reflected pulses. T corresponds to the time spacing between reflected or transmitted pulses and τ to the propagation time corresponding to one section. [18]

At this point, we have all the necessary conditions to recover the impedance for each section using the DLP algorithm. But, before performing this operation, we need to ensure that the reflection spectrum satisfies some conditions. The next section is devoted to the conditions that we need to guaranteed in order to realize a DTL.

2.3.2.1 Realization spectrum for DNTL structure

Before we start with the realizability conditions, it is important to review some important relations between analogue domain and digital domain. In this way, lets us start distinguishing *digital domain* and *analogue domain* concepts.

Analogue domain indicates something mathematically represented as a function of continuous variables, while digital domain is referred as a function of discrete independent variables. As illustrated in Figure 2.16, a discrete signal , $r(t)$, is obtained multiplying the continuous signal, $h(t)$, by a train of pulses at a certain frequency. In the frequency domain, this operation corresponds to a periodicity of the original spectrum, $H(\omega)$, with period 2π. In fact, the spectrum periodicity is a characteristic of all discrete systems. The frequency content results from the operation $\sum_{n=0}^{\infty} \delta[t-n]h(t)$ as illustrated in Figure 2.16(d).

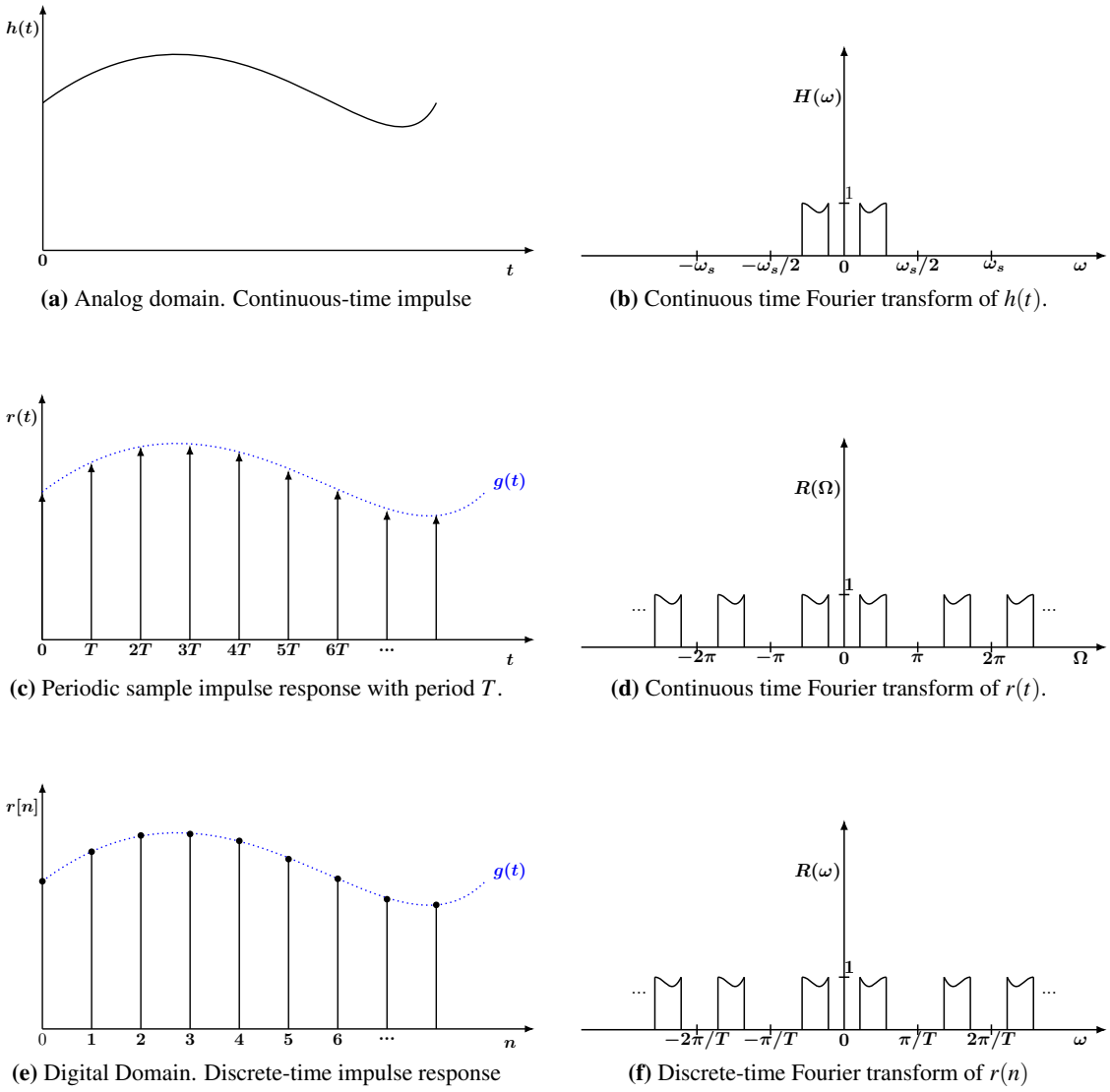

(a) Analog domain. Continuous-time impulse

(b) Continuous time Fourier transform of $h(t)$.

(c) Periodic sample impulse response with period T.

(d) Continuous time Fourier transform of $r(t)$.

(e) Digital Domain. Discrete-time impulse response

(f) Discrete-time Fourier transform of $r(n)$

Figure 2.16: Relationship between analog domain and digital domain.

In many applications, there is a significant advantage in processing the signal in the digital domain, and clearly Inverse Scattering is on of them.

We have presented a brief relationship between analogue and digital signal, but the main purpose of this section is to present the realizability conditions that the reflection spectrum (input data to the DLP) must satisfy in order to be realizable as a DNTL structure with a prescribed number of sections. Let us start by establishing the relation between z, which is the digital variable, and Ω according to the following equation:

$$z = re^{j\Omega}, \tag{2.21}$$

where r is the magnitude of z in the $z-plane$ and Ω is the frequency variable.

For the purposes of this section, reflection and transmission scattering are defined as

$$R(\Omega) = S_{11}(\Omega) \tag{2.22}$$

$$R(-\Omega) = R^{*}(\Omega). \tag{2.23}$$

$$T(\Omega) = S_{21}(\Omega) \tag{2.24}$$

Due to causality, the impulse response sequence, $r(n)$, for the DNTL structure must verify

$$r(n) = 0, n < 0, \tag{2.25}$$

where $r(n)$ is the inverse Fourier transform of $R(\Omega)$.

In order to guarantee equal impedance termination, the target spectrum must verify

$$R(\Omega = 0) = 0, n < 0, \tag{2.26}$$

In the $z-domain$ this means that $R(z)$ must have a zero at $z = e^{j0} = 1$.

For the lossless case, i.e., ideal transmission structure, and considering that the structure is a passive device, another realizability condition for the target spectrum arises from the law of conservation of energy, namely

$$0 \leq |R(\Omega)|^2 \leqslant 1, \forall\Omega \tag{2.27}$$

Another realizability condition comes as a stability condition. The stability conditions are set through the analysis of the z-Transform of the target spectrum $R(z)$. All poles of $R(z)$ must lie inside the unit circle.

All realizable reflection spectra $R(z)$ can be expressed by a rational function, in the form

$$R(z) = \frac{\beta_0 + \beta_1 z^{-1} + ... + \beta_{m-1} z^{-(m-1)} \beta_m z^{-m}}{\alpha_0 + \alpha_1 z^{-1} + ... + \alpha_{m-1} z^{-(m-1)} \alpha_m z^{-m}} \tag{2.28}$$

where the coefficients α_i and β_i are real. The stability and causality conditions require all roots of the denominator to lie inside of the unit circle.

From this analysis we can conclude that if our purpose is to synthesise a DTL using DSP techniques, the first step consists in an approximation of the reflection spectrum in an all-pole transfer function. In order to do this, in the present work the *parametric modelling tools* available

in Matlab will be used to obtain the coefficients β_m and α_m related to the (Equation (2.28)) or a_i and b_i in (Equation (2.29)).

The parametric modelling function can be divided in two groups: time-domain based modelling and frequency-domain based modelling The time domain modelling is based in the impulse response of the unknown system - the system to be approximated - while the frequency-domain is performed from the frequency response of the unknown system. Some of the time-domain based Matlab parametric modelling functions are *arburg*, *lpc*, *arcov*, *aryule*, *prony* and *stmcb*. On the other hand, the frequency-domain parametric modelling can be performed by the function *invfreqz*.

2.3.2.2 The Discrete Layer Peeling Procedure and Schur Recursions

From the previous section we know that a close relationship exists between a DNTL structure and digital signal processing theory. Taking advantage of digital signal processing techniques, namely existing DSP tools and the Z-Transform, we can improve the efficiency of the DLP algorithm. Therefore, from stand point of DSP we can summarize the DLP algorithm in the following simple steps:

1. Specify the target reflection spectrum in z-domain as the ratio of two polynomials of the order m. Thus for i=0,

$$R_0(z) = \frac{B(z)}{A(z)} = \frac{\sum_{i=0}^{m} b_i z^{-i}}{\sum_{i=0}^{m} a_i z^{-i}}, \tag{2.29}$$

   where m is the number of discrete impedance sections, and a_i and b_i are the real coefficients generated from parametric modelling tools.

2. Calculate the local reflection coefficient Γ_i on the interface between section $i-1$ and i through

$$\Gamma = \frac{b_0}{a_0}, \tag{2.30}$$

   that is, the ratio of the first $R(z)$ numerator and denominator respectively.

3. Compute the reflection response at the beginning of the next layer recursively in the following way.

$$R_{i+1}(z) = \frac{R_i(z) - \Gamma_i}{1 - \Gamma_i R_i(z)} \tag{2.31}$$

4. Peel off layer i.

5. As said in steps 2 and 3, the reflection coefficient must be calculated recursively. This means that this step must be repeated until the number of impedance sections, m is reached.

After conclusion of the 5 steps, we can easily calculate the impedance of each section using the following equation

$$Z_{0_i} = Z_{0_{i-1}} \frac{1+\Gamma_i}{1-\Gamma_i} \tag{2.32}$$

where Z_0, corresponds to the impedance of section $i = 0$, which is typically $50\,\Omega$.

The theoretical concepts related to the DLP and IS were presented. From hereon, the reader will be forwarded to this topic if necessary. For an more detailed review, please see [18].

2.4 Summary

In this chapter, an introduction to some Transmission Line concepts was presented. The RFID architecture and all of its main components were presented and described. Subsequently, the importance of antennas, voltage controlled oscillators, amplifiers, mixers, filters and digital to analogue converters, were briefly discussed. Additionally, tag related concepts, which constitute a central role in this work, were presented.

Also, a review of the Inverse Scattering method, which leads to the reconstruction of the physical properties of an unknown system from its reflection spectrum, was performed. Furthermore, a theoretical introduction to the DLPA, which is an efficient Inverse Scattering (IS) solution, was presented. Unlike the integral equation solution, the DLPA is an interactive solution that takes advantage of existent digital computation tools.

Chapter 3

System Design and Simulation

In this Chapter, some Microstrip Transmission Line (MTL) design considerations are discussed. These considerations must be taken into account in the tag's design procedures, in order to minimize the errors obtained by the DLPA. Therefore, simulation results that help us to choose the maximum and minimum impedance values, i. e, the optimal impedance range that are possible to be encoded and decoded with acceptable errors, are presented.

Next, implementation results of the Discreet Layer-Peeling Algorithm (DLPA) in Matlab, for the three different fitting methods considered in this work (*prony*, *stmcb* and *invfreqz*), are presented. In a first instance, the correct implementation of the algorithm will be validated considering ideal Transmission Lines (TL) simulations using the electromagnetic simulator ADS. Additionally, the performance characterization under noise, considering electromagnetic momentum simulations are presented and discussed.

Lastly, design and simulation results of printed disc UWB antennas are considered. The printed circular disc monopole antenna, was chosen because it is easier to design and it offers a very good bandwidth with minimal radiation distortion. To simulate the antenna, the electromagnetic simulator FEKO was used .

3.1 Microstrip Transmission Lines Design Considerations

So far, we have been speaking about Transmission Lines (TL) in general sense. However, in the present work, the used TL to the design of the proposed tag are the Microstrip Transmission Lines (MTL). Therefore, now, the most important equations to the design of MTL, as well, some practical considerations are presented. Figure 3.1 illustrates the $3D$ view of an MTL.
The characteristic impedance, Z_0, of an MTL mode, is given by Equation (3.1) [20]:

$$Z_0 = \begin{cases} \dfrac{60}{\sqrt{\varepsilon_e}} \ln\left(\dfrac{8d}{W} + \dfrac{W}{4d}\right), & \text{for } W/d \leq 1 \\ \dfrac{120\pi}{\sqrt{\varepsilon_e}\left[W/d + 1.393 + 0.667 \ln\left(W/d + 1.444\right)\right]}, & \text{for } W/d \geq 1 \end{cases} \tag{3.1}$$

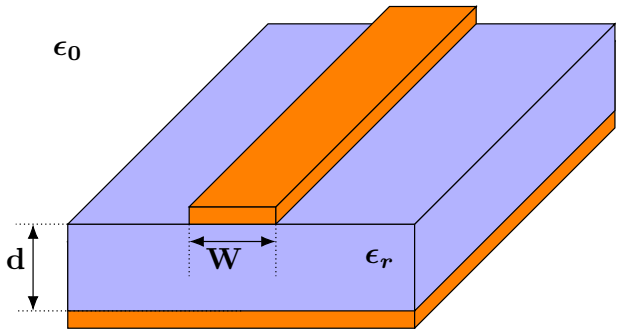

Figure 3.1: Schematic of a Microstrip Transmission Line (MTL) structure where, d is the dielectric height, W is the line width, ε_r is the relative dielectric permittivity and ε_0 is the free space permittivity.

where,

$$\varepsilon_e = \begin{cases} \dfrac{\varepsilon_r+1}{2} + \left[\dfrac{\varepsilon_r-1}{2}\dfrac{1}{\sqrt{1+12d/W}} + 0.004\left(1-\dfrac{d}{W}\right)^2\right], & \text{for } W/d \leq 1 \\ \dfrac{\varepsilon_r+1}{2} + \dfrac{\varepsilon_r-1}{2}\dfrac{1}{\sqrt{1+12d/W}}, & \text{for } W/d \geq 1 \end{cases} \tag{3.2}$$

is the effective dielectric permittivity, W is the line width and d is the dielectric high. The effective dielectric permittivity models the fact that the electric fields, E, does not exits totally inside of the TL as illustrated in Figure 3.5. It is possible to observe that some electrical field lines travel in air before its penetration in the substrate. Thus, the effective dielectric permittivity models an homogeneous medium characterized by ε_e, as illustrated in Figure 3.6.

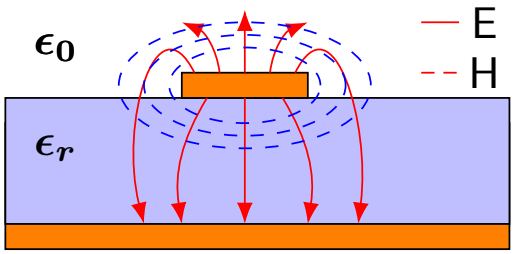

Figure 3.2: Electric and Magnetic field illustration of the quasi TEM mode of an MTL.

.

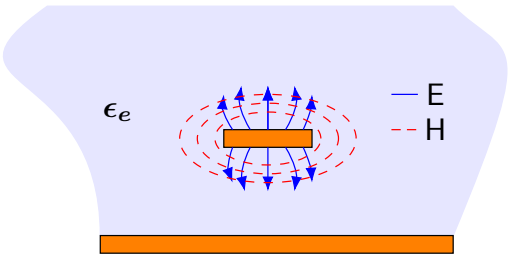

Figure 3.3: Electric and Magnetic field line distribution of an MTL in an homogeneous medium.

.

Equations (3.1) and (3.6) can be combined and rewritten as a function of the characteristic

impedance, Z_0, and the dielectric constant, ε_r, resulting in Equation (3.7). Therefore, the design specifications of an MTL are completely described by Equations (3.1) and (3.7).

$$\frac{W}{d} = \begin{cases} \dfrac{8e^A}{e^{2A}-2}, & \text{for } W/d < 2 \\ \dfrac{2}{\pi}\left[B-1-\ln(2B-1)+\dfrac{\varepsilon_r-1}{2\varepsilon_r-1}\left\{\ln(B-1)+0.39-\dfrac{0.61}{\varepsilon_r}\right\}\right], & \text{for } W/d > 2 \end{cases} \tag{3.3}$$

where,

$$A = \frac{Z_0}{60}\sqrt{\frac{\varepsilon_r+1}{2}} + \frac{\varepsilon_r-1}{\varepsilon_r+1}\frac{1}{\left(0.23+\dfrac{0.11}{\varepsilon_r}\right)}, \tag{3.4}$$

$$B = \frac{377\pi}{2Z_0\sqrt{\varepsilon_r}}. \tag{3.5}$$

Figure 3.7, represents the impedance as a function of the line widths, W, considering the dielectric height, d, 0.813 mm and the dielectric relative permittivity, ε_r, 3.38. The line widths were calculated for three different frequencies using the ADS LineCalc. The evaluated frequencies were 2.5 GHz with triangular shape marker, 5 GHz with asterisk shape marker, 10 GHz with circle shape marker and the "theoretical", obtained from Equation (3.7), labeled with continues trace shape marker. As it is possible to observe, between 0 to 15 mm, the "theoretical" curve and the curves obtained using the ADS LineCalc tool are in very good accordance and they are independent of the designed central frequency, F_c.

Also, from Figure 3.7, it is possible to see that for very high impedances, the line width varies slowly. Thus, the physical dimension of the high impedances are very close to each other. This fact, requires high quality level manufacture process, otherwise the errors obtained by the DLPA will be unacceptable. On the other hand, the line width tends to be very large as the impedance decreases and, this fact make the tag very large, which is not desire. Additionally, as the line width increases the radiation loss increases, which increase the errors in the decoding process.

where,

$$\varepsilon_e = \begin{cases} \dfrac{\varepsilon_r+1}{2} + \left[\dfrac{\varepsilon_r-1}{2}\dfrac{1}{\sqrt{1+12d/W}} + 0.004\left(1-\dfrac{d}{W}\right)^2\right], & \text{for } W/d \leq 1 \\ \dfrac{\varepsilon_r+1}{2} + \dfrac{\varepsilon_r-1}{2}\dfrac{1}{\sqrt{1+12d/W}}, & \text{for } W/d \geq 1 \end{cases} \tag{3.6}$$

is the effective dielectric permittivity, W is the line width and d is the dielectric high. The effective dielectric permittivity models the fact that the electric fields, E, does not exits totally inside of the TL as illustrated in Figure 3.5. It is possible to observe that some electrical field lines travel in air before its penetration in the substrate. Thus, the effective dielectric permittivity models an homogeneous medium characterized by ε_e, as illustrated in Figure 3.6.

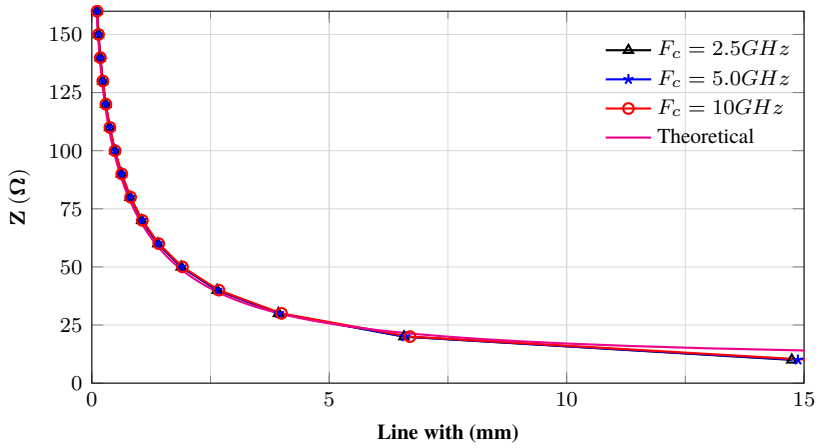

Figure 3.4: Transmission line characteristic impedances as a function of the line width for a lossless MTL implementation with zero thickness perfect conductor metal layers. The substrate properties are: dielectric height, $d = 0.813$ mm, relative permittivity, $\varepsilon_r = 3.38$ and $\tan\delta = 0$.

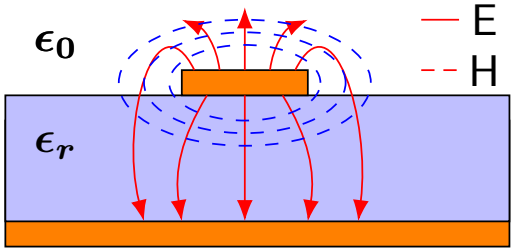

Figure 3.5: Electric and Magnetic field illustration of the quasi TEM mode of an MTL.

.

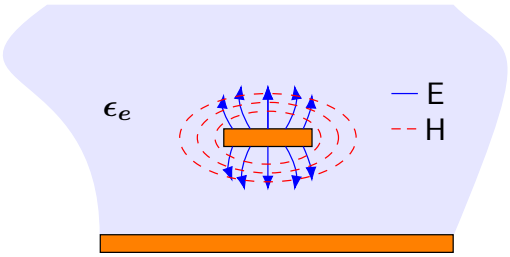

Figure 3.6: Electric and Magnetic field line distribution of an MTL in an homogeneous medium.

.

Equations (3.1) and (3.6) can be combined and rewritten as a function of the characteristic impedance, Z_0, and the dielectric constant, ε_r, resulting in Equation (3.7). Therefore, the design specifications of an MTL are completely described by Equations (3.1) and (3.7).

$$\frac{W}{d} = \begin{cases} \dfrac{8e^A}{e^{2A}-2}, & \text{for } W/d < 2 \\ \dfrac{2}{\pi}\left[B - 1 - \ln(2B-1) + \dfrac{\varepsilon_r - 1}{2\varepsilon_r - 1}\left\{\ln(B-1) + 0.39 - \dfrac{0.61}{\varepsilon_r}\right\}\right], & \text{for } W/d > 2 \end{cases} \tag{3.7}$$

where,

$$A = \frac{Z_0}{60}\sqrt{\frac{\varepsilon_r + 1}{2}} + \frac{\varepsilon_r - 1}{\varepsilon_r + 1}\frac{1}{\left(0.23 + \frac{0.11}{\varepsilon_r}\right)}, \tag{3.8}$$

$$B = \frac{377\pi}{2Z_0\sqrt{\varepsilon_r}}. \tag{3.9}$$

Figure 3.7, represents the impedance as a function of the line widths, W, considering the dielectric height, d, 0.813 mm and the dielectric relative permittivity, ε_r, 3.38. The line widths were calculated for three different frequencies using the ADS LineCalc. The evaluated frequencies were 2.5 GHz with triangular shape marker, 5 GHz with asterisk shape marker, 10 GHz with circle shape marker and the "theoretical", obtained from Equation (3.7), labeled with continues trace shape marker. As it is possible to observe, between 0 to 15 mm, the "theoretical" curve and the curves obtained using the ADS LineCalc tool are in very good accordance and they are independent of the designed central frequency, F_c.

Also, from Figure 3.7, it is possible to see that for very high impedances, the line width varies slowly. Thus, the physical dimension of the high impedances are very close to each other. This fact, requires high quality level manufacture process, otherwise the errors obtained by the DLPA will be unacceptable. On the other hand, the line width tends to be very large as the impedance decreases and, this fact make the tag very large, which is not desire. Additionally, as the line width increases the radiation loss increases, which increase the errors in the decoding process.

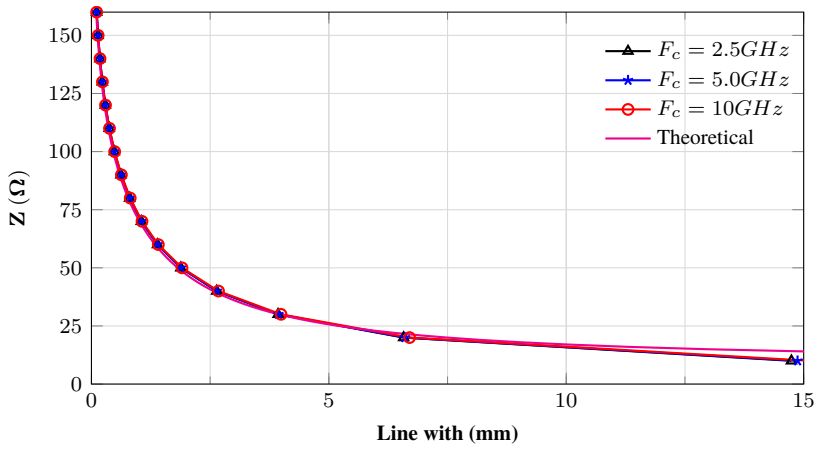

Figure 3.7: Transmission line characteristic impedances as a function of the line width for a lossless MTL implementation with zero thickness perfect conductor metal layers. The substrate properties are: dielectric height, $d = 0.813$ mm, relative permittivity, $\varepsilon_r = 3.38$ and $\tan\delta = 0$.

In this section, we have concluded that the line width of the microstrip line does not depend of the frequency. However, the length of the line does depend on the design frequency, F_c. According to the results obtained considering in ADS momentum, different values of impedance have different lengths, even if we consider the design frequency as constant. Table 3.1 illustrate an example

of we are trying to explain, in which, under ideal condition the physical-length should be constant, however, in practice this is not verified. This dependence is explained by Equations (3.10) and (3.11) considering a MTL with zero thickness conductor, uniform dielectric material and infinite ground plane [20].

Table 3.1: Variation of the length of the line the characteristic impedance impedance considering constant design frequency.

Impedance (Ω)	Design Frequency (GHz)	Physical Length (mm)
10	10	9.718500
20	10	9.691250
30	10	9.660130

$$\gamma = \beta = \omega\sqrt{\mu_0 \varepsilon_0 \varepsilon_e} \tag{3.10}$$

$$\phi = \beta l_{phy} \tag{3.11}$$

where γ is the propagation constant, β is the phase constant in radian per meter, μ_0 is the free space permeability, ε_0 is the free space permittivity, ε_e is the effective permittivity, ω is the angular frequency in radian, ϕ is the electric length in degrees and l_{phy} is the physical length in meters. Combining Equations (3.10) and (3.11) result that,

$$l_{phy} = \frac{\phi^o \pi / 180^o c}{2\pi f \sqrt{\varepsilon_e}}, \tag{3.12}$$

where c is free space light speed. Replacing Equation (3.6) in Equation (3.12), results in Equation (3.13), where the frequency dependence of the physical length appears.

Figure 3.8 depicts the physical length calculated for three different frequencies using the ADS LineCalc tool.

$$l_{lphy} = \begin{cases} \dfrac{\phi^o c}{360 f} \dfrac{1}{\sqrt{\varepsilon_r/2 + 1/2 + 1/2(\varepsilon_r - 1)\dfrac{1}{\sqrt{1 + 12\dfrac{d}{W}}} + 0.0004\left(1 - \dfrac{d}{W}\right)^2}}, & \text{for } W/d \leq 1 \\ \dfrac{\phi^o c}{180 f} \dfrac{1}{\sqrt{2\varepsilon_r + 2 + 2(\varepsilon_r - 1)\dfrac{1}{\sqrt{1 + 12\dfrac{d}{W}}}}}, & \text{for } W/d \geq 1 \end{cases} \tag{3.13}$$

At this moment, it is possible to conclude that to choose of a high operattion frequency to the design of the tag has a positive benefit in the sense that it allows us to reduce the size of the tag. However, in order to develop a competitive tag, several aspects must be taken into account. Theretofore, a high central frequency gives rive to another problems that must be considered, as for example, the requirement for very good manufacture process, expensive components for the

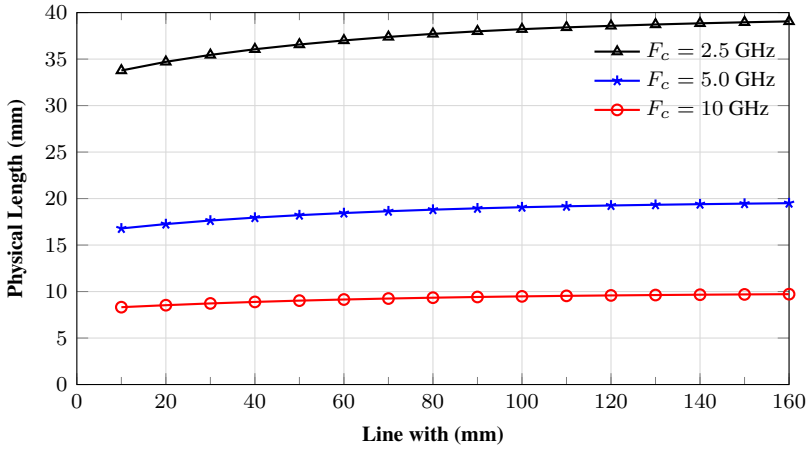

Figure 3.8: Transmission line physical length as a function of the line width for a lossless MTL implementation with zero thickness perfect conductor metal layers. The substrate properties are: dielectric height, $d = 0.813$ mm, relative permittivity, $\varepsilon_r = 3.38$, $\tan\delta = 0$ and electric length, ϕ, 180^0.

RFID transceiver and expensive dielectric material capable to operate at very high frequency with acceptable quality.

Figures 3.9 and 3.10 depict the impedance value, Z_0, for different values of permittivity, ε_r, and dielectric height, d, respectively, which are important to conclude that the physical dimension of the tag also depends of the characteristics of the dielectric material.

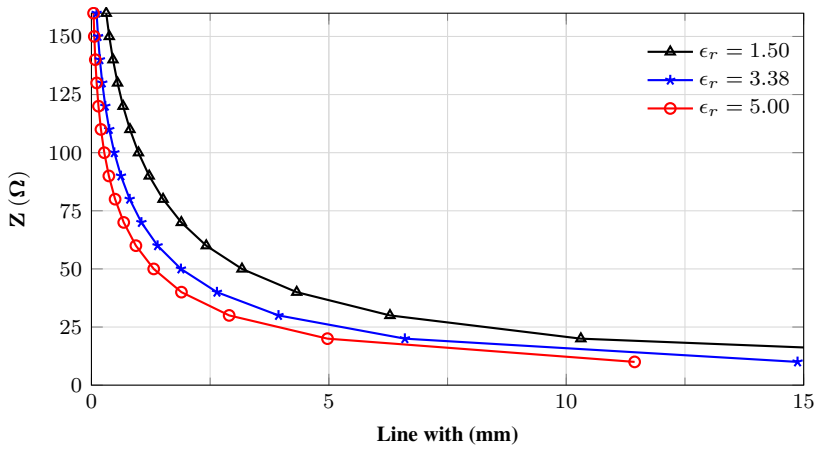

Figure 3.9: Transmission line characteristic impedances as a function of the line width for a lossless MTL implementation with zero thickness perfect conductor metal layers considering three different values of ε_r. The substrate properties are: dielectric height, $d = 0.813$ mm and $\tan\delta = 0$.

So far, we have considered that the lossless dielectric materials. However, in practice, losses of energy are inevitable. In Microwave Engineering, according to the law of conservation of energy, the magnitude of the transmission and Reflection Coefficients should satisfies the Equation (3.14).

$$|S_{11}|^2 + |S_{21}|^2 = 1 \tag{3.14}$$

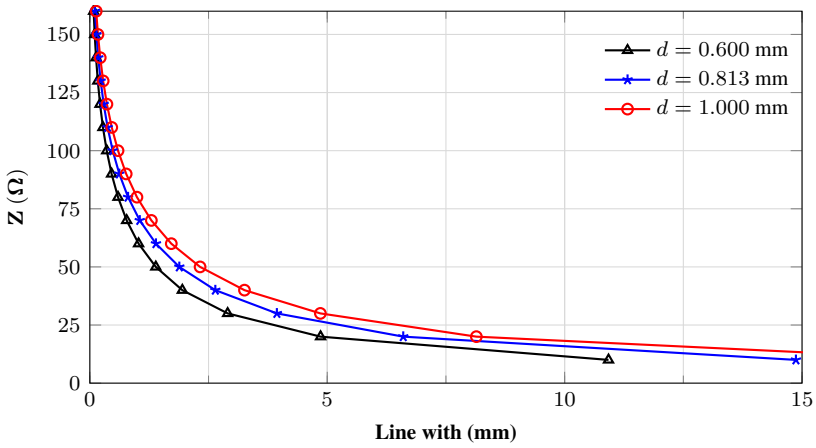

Figure 3.10: Transmission line characteristic impedances as a function of the line width for a lossless MTL implementation with zero thickness perfect conductor metal layers considering three different values of dielectric height, d. The substrate properties are: relative permittivity, $\varepsilon = 3.38$ and $\tan\delta = 0$.

However, due to the loss, Equation (3.14) must be compensated as follows,

$$|S_{11}|^2 + |S_{21}|^2 = 1 - PLF, \tag{3.15}$$

resulting that,

$$PLF = 1 - |S_{11}|^2 - |S_{21}|^2. \tag{3.16}$$

where PLF means Power Loss Factor.

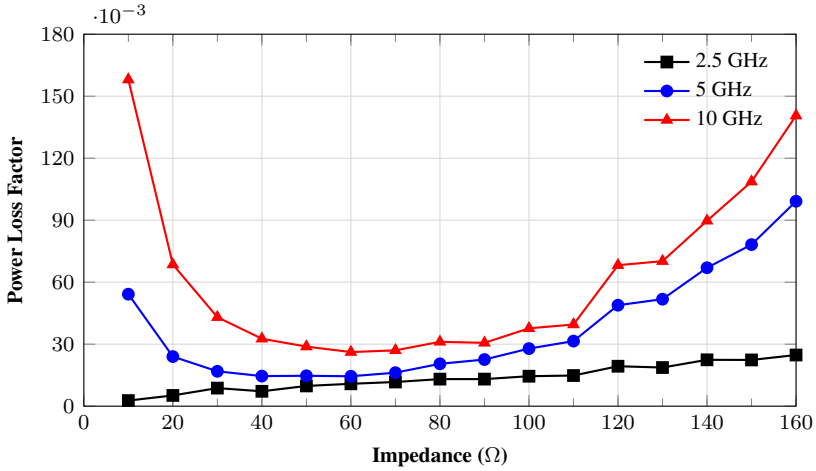

Figure 3.11: Power loss factor as a function of the impedance for a lossless MTL implementation three different values of frequencies. The substrate properties are: dielectric height, $d = 0.813$ mm and $\tan\delta = 0.003$ and $\phi = 180^o$.

Figure 3.11 represents the total PLF losses such as, the radiation loss and conductor loss. As it is possible to see, for small impedances values (below 20 Ω) the PLF is higher than that at around 60 Ω. With small impedances, the main source of losses are the radiations effects. (please see Figures 3.12 and 3.13). This is due to the fact that, the TL starts to operate as a Microstrip patch

antenna at certain width. In order to better understand and visualise the radiation loss mechanism and its dependence with the line width and frequency, ML with different widths were simulated considering the dielectric height, d, 0.813 mm permittivity, ε_r, 3.38 and Perfect Electric Conductor (PEC). The results are depicted in Figures 3.12 and 3.13 and they are in accordance with Figure 3.11. On the other hand, the conductor loss and the dielectric loss increase as the impedance increases. These different loss mechanisms explain the "valley curves" (with maximums at the extremes and minimum at the center) illustrated in Figure 3.11. The variation of the losses with the physical geometry of the impedances and frequency gives rise to magnitude distortion and non-linearities, which increases the errors obtained by the DLP. In order to minimize this problem, the encoding impedance range must be between 20 Ω to 110 Ω, where the losses are approximately constant.

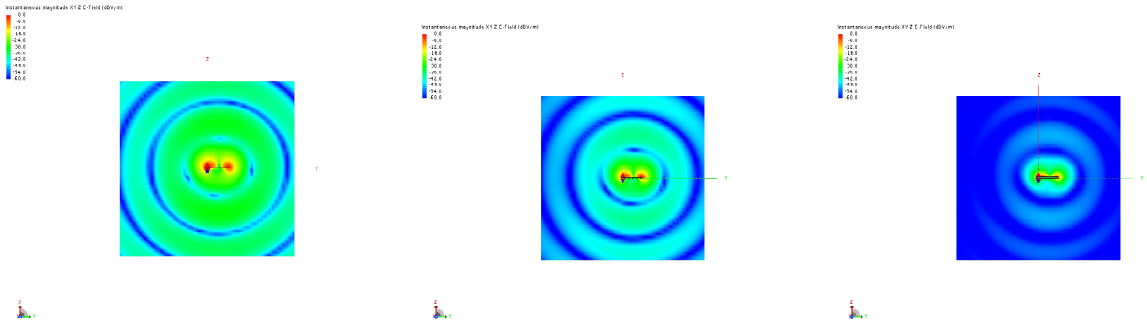

Figure 3.12: Illustration of the radiation loss effect considering the line width equal to 10, 5 and 1 mm from left to the right respectively at 5 GHz. The Electric Field are normalized and in dB. The transmission line was simulated in FEKO.

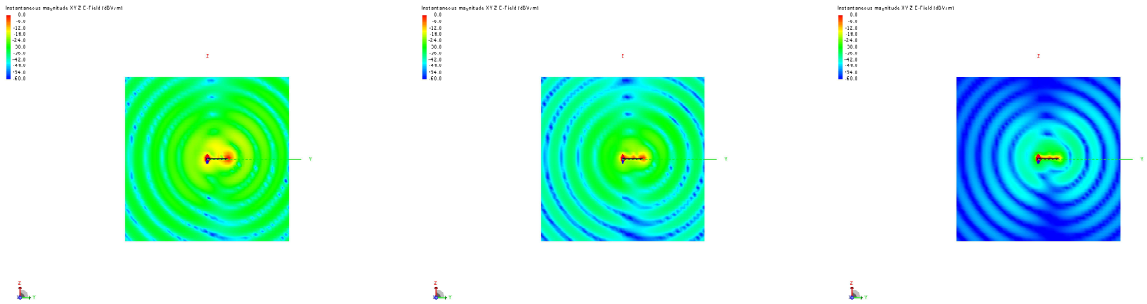

Figure 3.13: Illustration of the radiation loss effect considering the line width equal to 10, 5 and 1 mm from left to the right respectively at 10 GHz. The Electric Field are normalized and in dB. The transmission line was simulated in FEKO.

3.2 Discrete Layer-Peeling Algorithm Implementation

According to the Section 2.3.2.2, the DLPA can be summarized in the flow chart presented in Figure 3.14. The 1^{th} step, is to compute the coefficients b_0, b_1, ..., b_m and a_0, a_1, ..., a_m of the numerator and denominator of the Equation (2.29). To obtain them, may be used: *invfreqz*, *prony*

and *stmcb*, all available in MATLAB. These methods receive the Reflection Spectrums, $S_{11}(\omega)$, of a desirable impedance profile and provide the coefficients of a rational Z-Transfer function that best fit the original Reflection Spectrum. The order of the transfer function is defined by the number of impedance sections. The $S_{11}(\omega)$ can be obtained theoretically from Equation (2.4), or using on electromagnetic simulator like ADS, HFSS or FEKO. In fact, the use of the theoretical equation to obtain the Reflection Spectrum is very limited because it is an ideal equation that does not take into account phenomena that occurs in practice, as for example, radiation effect, subtract loss and conductor loss. However, in order to obtain preliminary results and to achieve a better understanding of the DTL, it is important to consider it. MATLAB code developed to compute ideal TL spectrum is provided in Appendix A.1.

After obtaining the coefficients $b_0,\ b_1,\ ...,b_m$ and $a_0,\ a_1,\ ...,a_m$, of the Z-Transfer Function that correspond to the Reflection Spectrum, $S_{11}(Z)$, at the input of the 1^{th} impedance section, $i = 0$, the reflection coefficient, Γ_0, is obtained by the quotient between b_0 and a_0 according to Equation (2.30). At this point, we have discovered the first impedance section according to Equation (2.32). After that, the Reflection Spectrum at the input of the next section, $i+1$, is calculated using Equation (2.31), from which the reflection coefficient, Γ_1, is obtained. This process is repeated recursively until the number of impedance sections is reached and, at the end we have discovered the impedance of each section. Figure 3.14 demonstrate that, first we have to calculate the Reflection Coefficient at the interface of each sections, and lastly we compute all the impedances from them. However, the impedance of each can be calculated at the interaction *i* without previous knowledge of the next impedance sections. This means, layer by layer identification, which is the essence of the DLPA.

The DLPA was implemented in MATLAB and tested with Reflection Spectrum, $S_{11}(\omega)$, obtained with the simulator ADS. The encoded profile impedance that we used is illustrated in Figure 3.15. As it is possible to observe, the design central frequency of the TL sections is 5 GHz, which means that the spectrum has a periodicity of 5 GHz, as discussed in the previous Chapter. The magnitude and phase of the Reflection Spectrum are illustrated in Figure 3.16, in which the periodicity is evident. The coefficients of the Equation (2.29), that best fit the spectrum originally in the Frequency Domain are presented in Tables 3.3 and 3.4 and **??** for the methods *invfreqz, prony* and *stmcb* respectively. By inspection, it is possible to observe that the results produced by the methods *prony* and *stmcb* are identical. However, as we will see in Section 4.2, in practice all the methods produce different coefficients. Also, the pole-zero configurations of the Z-Transfer functionscorresponding to the different methods are presented in Figures 3.17 to 3.19. In Figure 3.20, comparison between the original $S_{11}(f)$, and $S_{11}(Z)$ are presented. As we can conclude, all the methods produce very good fitting curves.

The results obtained by the DLP are presented in Figures 3.21 and 3.22, in which Figure 3.21 corresponds to the Reflection Coefficient at the interface of each section and Figure 3.22 depicts the recovered impedances.

In summary, we can conclude that the algorithm was correctly implemented and produce very good results under ideal conditions.

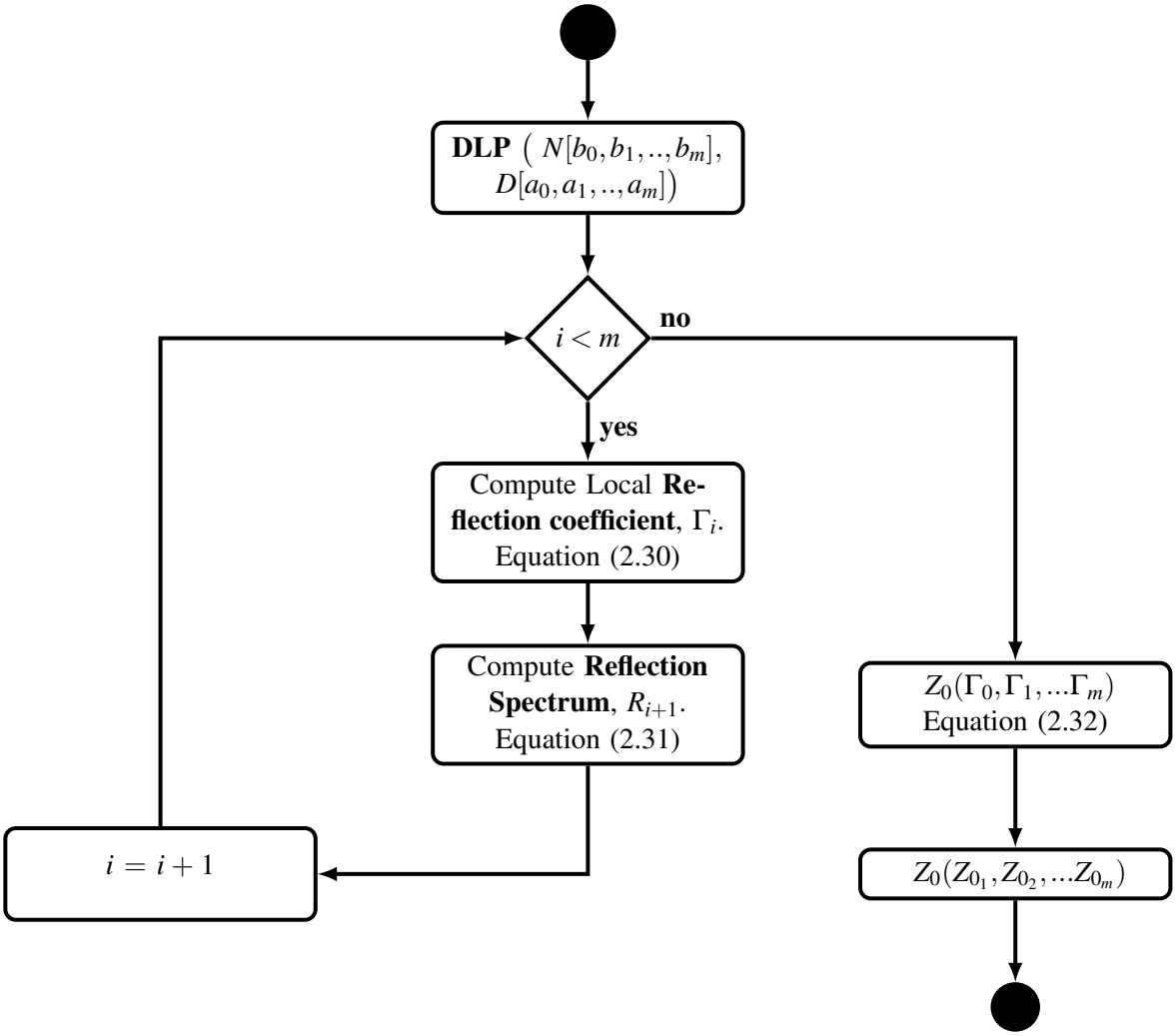

Figure 3.14: DLP algorithm flow chart.

Table 3.2: Coefficients of the 8*th* order reflection frequency $S_{11}(z)$ for the pole-zero configuration depicted in Figure 3.17.

Coefficientes		**invfreqz**	
Numerator	Denominator		
a_0	b_0	0.0909	1.0000
a_1	b_1	0.0374	-0.4280
a_2	b_2	0.1500	-0.3953
a_3	b_3	-0.0079	0.4118
a_4	b_4	-0.8016	-0.0816
a_5	b_5	0.5767	-0.0116
a_6	b_6	0.2707	0.0163
a_7	b_7	-0.4274	-0.0304
a_8	b_8	0.1111	0.0101

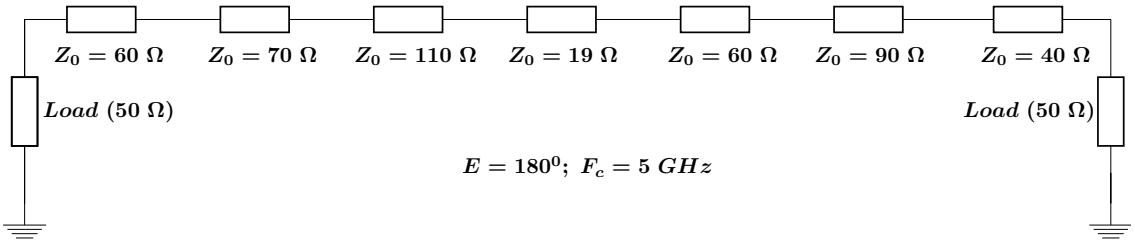

Figure 3.15: Ideal discrete transmission line.

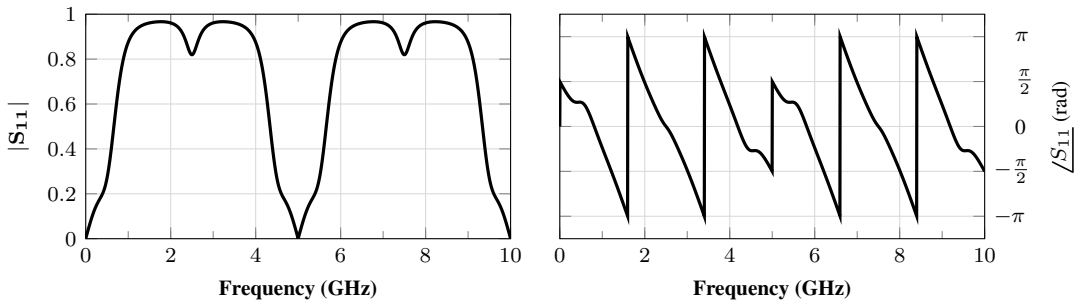

Figure 3.16: Magnitude and phase of the reflection spectrum corresponding to the transmission line depicted in Figure 3.15.

Table 3.3: Coefficients of the 8*th* order reflection frequency $S_{11}(z)$ for the pole-zero configuration depicted in Figure 3.17.

Coefficientes		**stmcb**	
Numerator	Denominator		
a_0	b_0	0.0909	1.0000
a_1	b_1	0.0374	-0.4280
a_2	b_2	0.1500	-0.3953
a_3	b_3	-0.0079	0.4118
a_4	b_4	-0.8016	-0.0816
a_5	b_5	0.5767	-0.0116
a_6	b_6	0.2707	0.0163
a_7	b_7	-0.4274	-0.0304
a_8	b_8	0.1111	0.0101

The performance of the algorithm in presence of noise, will be discussed in the next section considering momentum simulation obtained using ADS. Practical evaluation performance will be presented and discussed in Section 4.2.

Table 3.4: Coefficients of the 8*th* order reflection frequency $S_{11}(z)$ for the pole-zero configuration depicted in Figure 3.19.

Coefficients		**prony**	
Numerator	Denominator		
a_0	b_0	0.0902	1.0000
a_1	b_1	0.1778	1.1174
a_2	b_2	0.2639	-0.4318
a_3	b_3	0.2719	-0.2111
a_4	b_4	-0.6974	0.3027
a_5	b_5	-0.6260	0.0164
a_6	b_6	0.6758	0.0097
a_7	b_7	0.1579	-0.0081
a_8	b_8	-0.3147	-0.0282

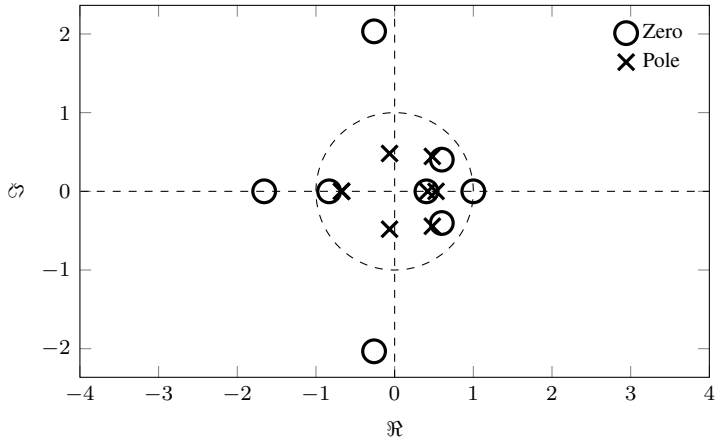

Figure 3.17: Polo-Zero configuration of the 8*th* order reflection spectrum $S_{11}(z)$ obtained using the *invfreqz* fitting method.

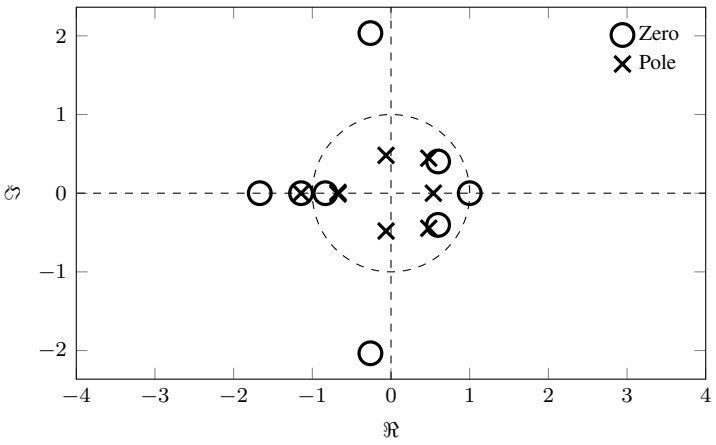

Figure 3.18: Polo-Zero configuration of the 8*th* order reflection spectrum $S_{11}(z)$ obtained using the *stcmb* fitting method.

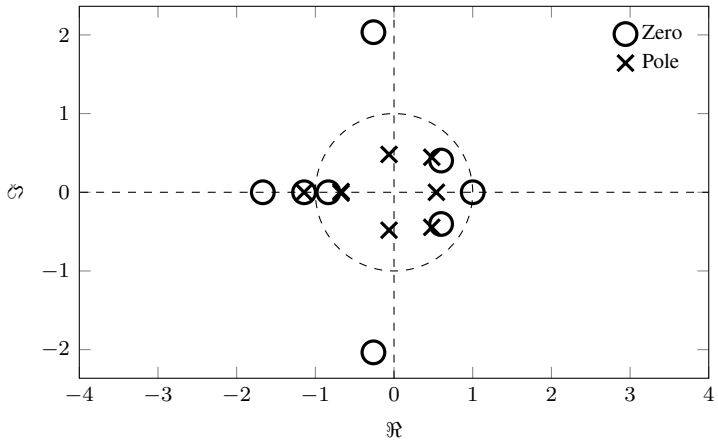

Figure 3.19: Polo-Zero configuration of the $8th$ order reflection spectrum $S_{11}(z)$ obtained from the *prony* fitting method.

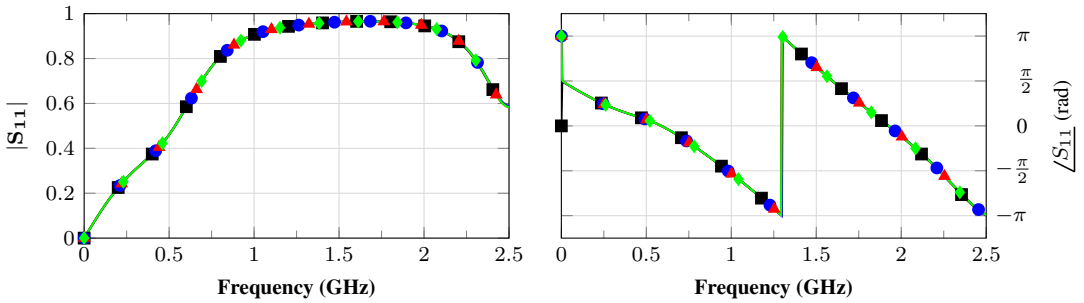

Figure 3.20: Fitting of the reflection spectrum presented in Figure 3.16 considering the methods *invefrez* with square shape marker, *prony* with circle shape marker and *stmcb* with triangle shape marker.

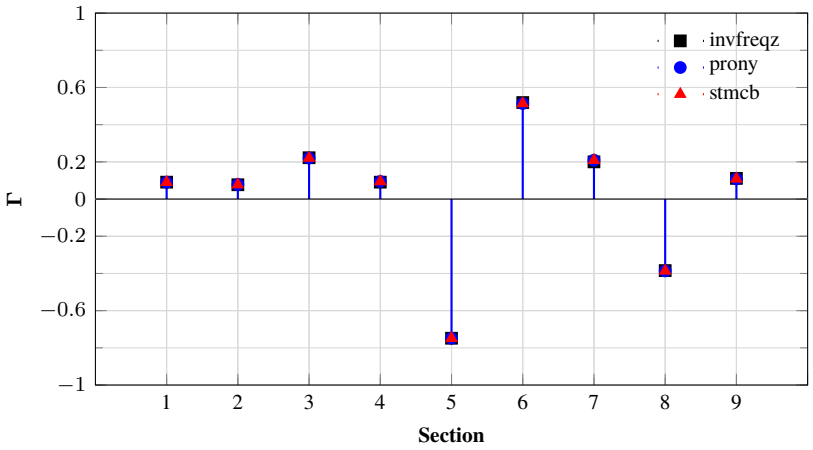

Figure 3.21: Reflection coefficients at the interface of the sections of the discrete transmission line illustrated in Figure 3.15. These reflection coefficients were obtained using the DLP algorithm.

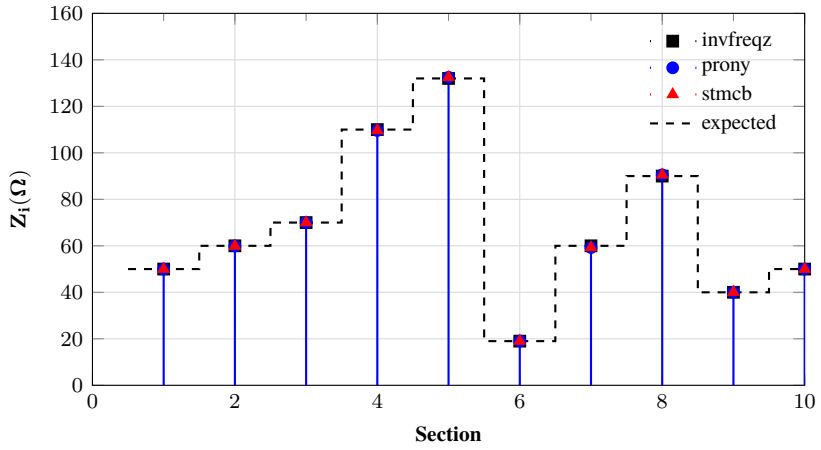

Figure 3.22: Recovered impedance using the DLP algorithm considering the ideal the discrete ideal transmission line illustrated in Figure 3.15

3.3 Performance Analysis of the DLP Considering non Ideal Transmission Line

In Section 3.1, it was seen that in practice TL have several nonidealities, as for example, radiation losses and substrate losses. These factors introduce distortion in the Reflection Spectrum, that will affect the performance of the DLPA.

???? illustrate Ideal Reflection Spectrum and comparison with *momentum simulation*, labeled with "Ideal" and "ADS momentum" respectively, both obtained in ADS. The impedances that correspond to the different Reflection Spectrums are mapped in Table 3.5, in which the impedance values corresponding to 20 Ω and 120 Ω were chosen because we consider them as the acceptable maximum and minimum values according to the conclusions obtained from Figure 3.11.

As it is possible to observe, as the number of impedance sections increase, the differences between "Ideal" and "ADS momentum" are greater. This observation is very important, in the sense that, it will define the maximum number of physical impedance sections that are possible to be encoded and decoded with acceptable error levels.

Table 3.5: Table of the encoded impedance values corresponding to the $S_1 1$ presented in **????**.

Figures	Encoded impedance
A	20
B	20-120
C	20-120-20
D	20-120-20-120
E	20-120-20-120-20
F	20-120-20-120-20-120
G	20-120-20-120-20-120-20
H	20-120-20-120-20-120-20-20
I	20-120-20-120-20-120-20-20-120
J	20-120-20-120-20-120-20-20-120-20
K	20-120-20-120-20-120-20-20-120-20-120
L	20-120-20-120-20-120-20-20-120-20-120-20

The recovered impedances corresponding to the Reflection Spectrums presented in **??** and **??** are depicted in Figure 3.23. As it was expected, the magnitude of the errors increase as the number of impedance sections increases. The impedances corresponding to the spectra of **??**, ere not considered because the were not considered because the obtained errors were to large.

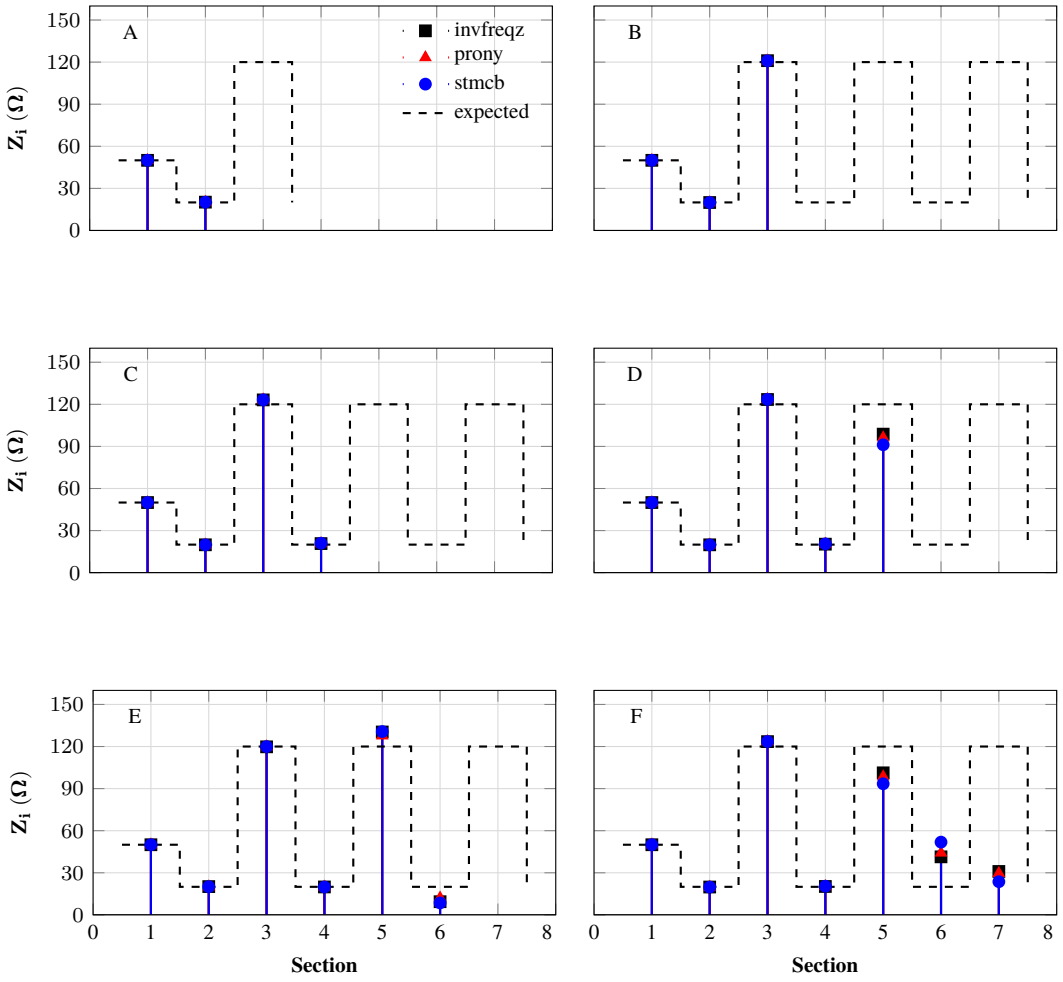

Figure 3.23: Recovered impedance corresponding to the reflection spectrums presented in **??** for the simulation obtained by the method of momentum.

3.4 Ultra Wide Band Antennas

Ultra-wideband (UWB) is a wireless technology that covers the frequency range from 2-10.6 GHz, which is based on large amounts of digital data at extremely low power for a short distance range. The UWB technology offers several advantages over conventional communications systems. For instance, there is no carrier frequency. Instead, UWB emits timed "pulses" of electromagnetic energy. Therefore, transmitter and receiver hardware can be made very simple, which is necessary for the portable devices. There is a wide range of applications for UWB technology, which includes wireless communication systems, UWB, microwave sensing imaging, and radar. In summary, Ultra-wideband technology has been used for high data rate, low cost, and low power. [2, 33]

The most common type of UWB antennas and easy to simulate, fabricate and that offers very high bandwidth with low radiation distortion, are: the printed circular monopole antenna, the printed triangular dipole antenna and the printed circular dipole antenna.

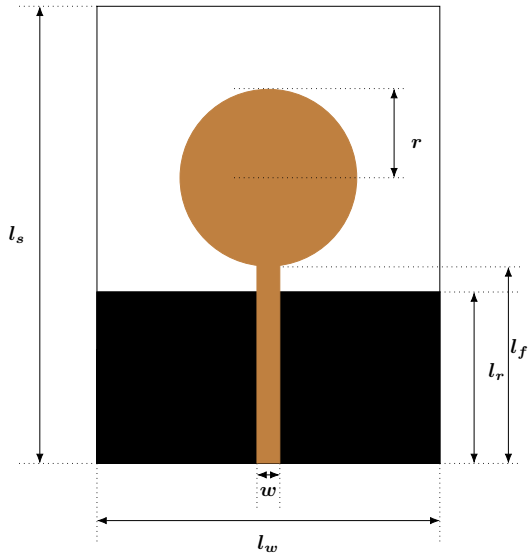

Figure 3.24: Technical drawing of the printed circular monopole antenna were, l_s is the substrate length, l_w is substrate width, w is the feed line width, l_r is the length of the reflector plane, l_f is the feed line length and r is the radius of the disc.

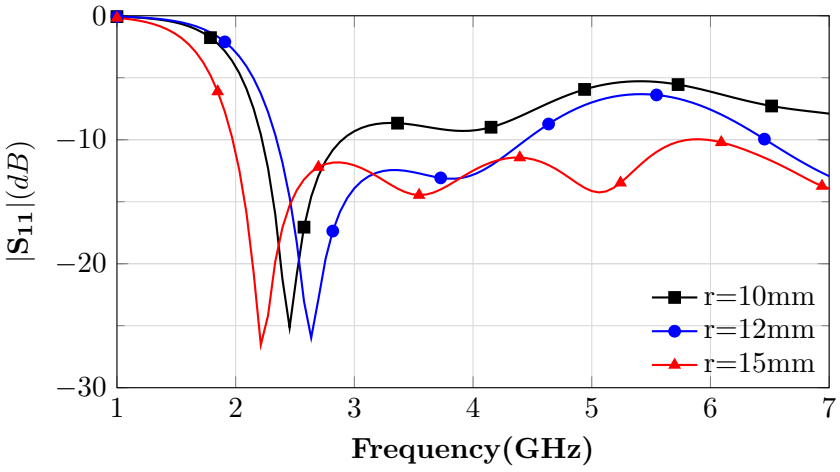

Figure 3.25: S_{11} of the antenna illustrated in Figure 3.24 considering, $w = 2.6$, $l_w = 20$, $l_s = 50$ mm, $l_f = 26.3$ and $r = 10, 12$ *and* 15.

The dipoles antennas offer a better impedance matching bandwidth and low radiation distortion. However, they present a very high input impedance (in order of 180 Ω), which requires additional matching. Furthermore, the use of dipole antennas in the proposed tag requires a Microstrip to CPW transition. Thus, the printed disc circular monopole (illustrated in Figure 3.24) antenna was chosen. It is easier to simulate, offers a good matching impedance bandwidth to 50 Ω, and small radiation distortion. To design it, the electromagnetic simulator in FEKO was used. We start by determining the width of the feeding line and the reflector plane dimension that guaranty a good impedance matching to 50 Ω, and later a parametric analysis of the radius was carried out.

The S_{11} simulation results for different radius are presented in Figure 3.25 and Figure 3.26 plots simulation results of the 3D Radiation Patterns for different frequencies. It is possible to

conclude that, the Radiation Patterns do not differ a lot from each other, which means that the radiation distortion is minimal.

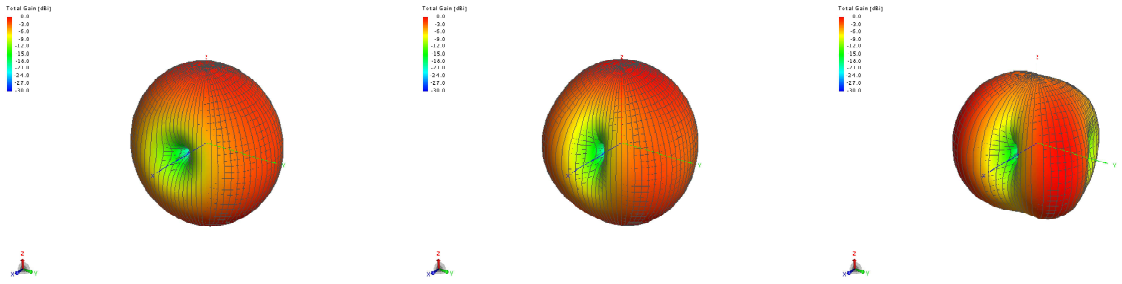

Figure 3.26: 3*D* radiation patterns of the antenna illustrated in Figure 3.24 considering $w = 2.6$, $l_w = 20$, $l_s = 50$, $l_f = 26.3$ and $r = 15$ for 3 4.5 and 6 GHz from left to the right, respectively. Note: all units are in mm.

3.5 Summary

In this Chapter, it was demonstrated that the DLP algorithm was successfully implemented. otionally, it was concluded that, practical consideration must be taken into account in the design procedure in order to minimize the errors obtained by the DLPA. In order to evaluate the performance of the algorithm in presence of noise and losses, simulations obtained by the *Method of Momentum* (MoM) was considered using the simulator ADS.

Lastly, results of a printed Circular disc antenna were presented and discussed. The design of the antenna was carried out using the electromagnetic simulator FEKO.

Chapter 4

Experimental Evaluation

4.1 Measurement Setup

In this section, the experimental procedures that were carried out in order to obtain the practical results are considered. The procedures involved the manufacture of two tags, and one printed circular disc monopole antenna.

4.1.1 Tags

In order to evaluate the performance of the DLP algorithm in a practical scenario, the experimental part of this work was started by manufacturing two different tags, previously designed in ADS. The manufactured tags are illustrated in Figures 4.1 and 4.2 corresponding to an 8 and 12 sections transmission line respectively, designed in Microstrip technology. In order to illustrate the relative dimension of the tag's, they are presented side by side with a ruler.

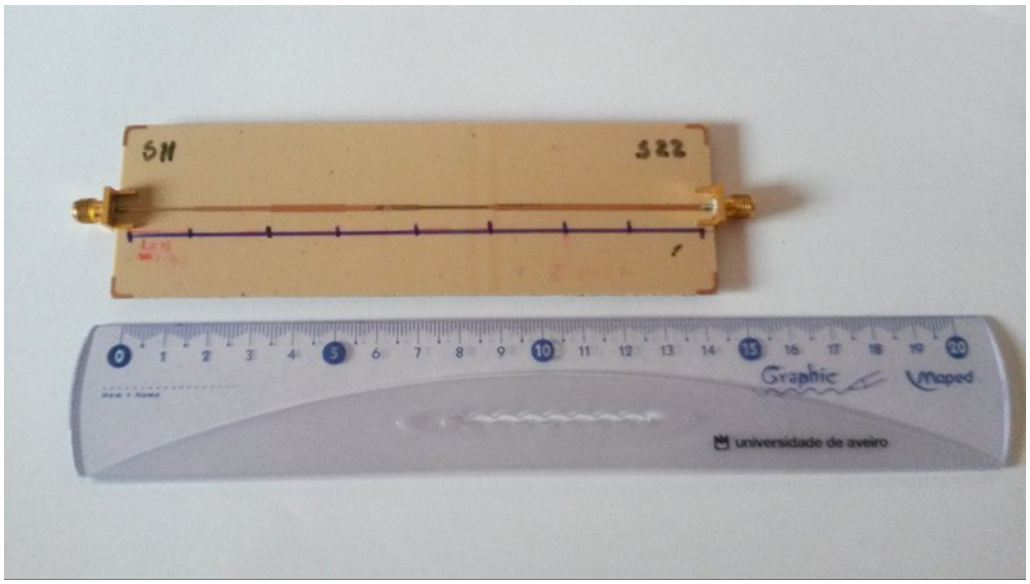

Figure 4.1: 8 section discrete MTL fabricated in the substrate Roger Duroid 4003C with dielectric permittivity, ε_r, 3.38 and dielectric hight, d, 0.813 mm.

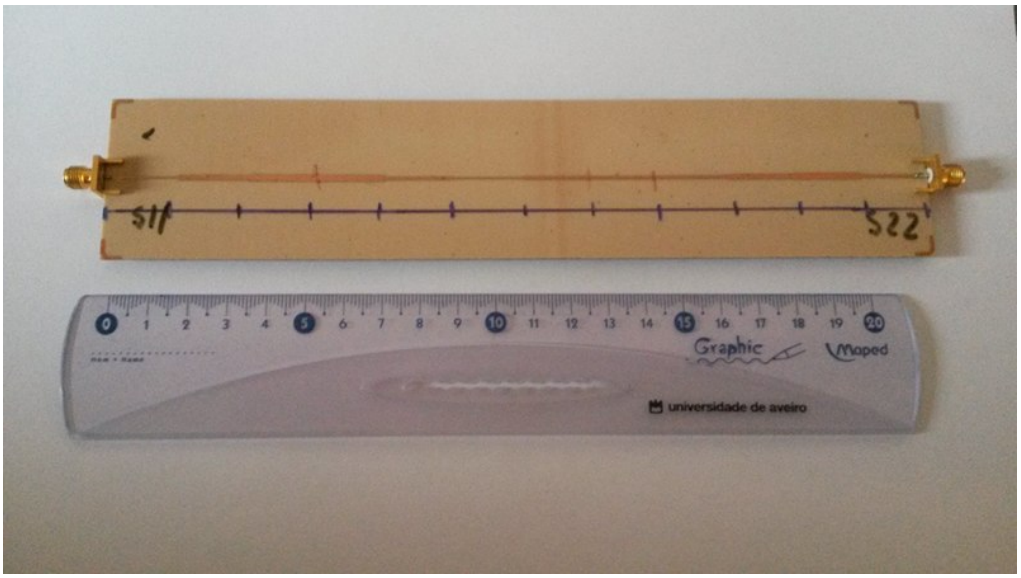

Figure 4.2: 12 section discreet MTL fabricated in the substrate Roger Duroid 4003C with dielectric permittivity, ε_r, 3.38 and dielectric hight, d, 0.813 mm.

4.1.2 UWB Antennas

The manufactured antenna is depicted in Figure 4.3. It was previously designed and simulated in FEKO. Simulation results and design procedures were discussed in Section 3.4. The radius of the disc is equal to 15 mm, and the feed line has 2.6 and 26.3 mm of width and length respectively.

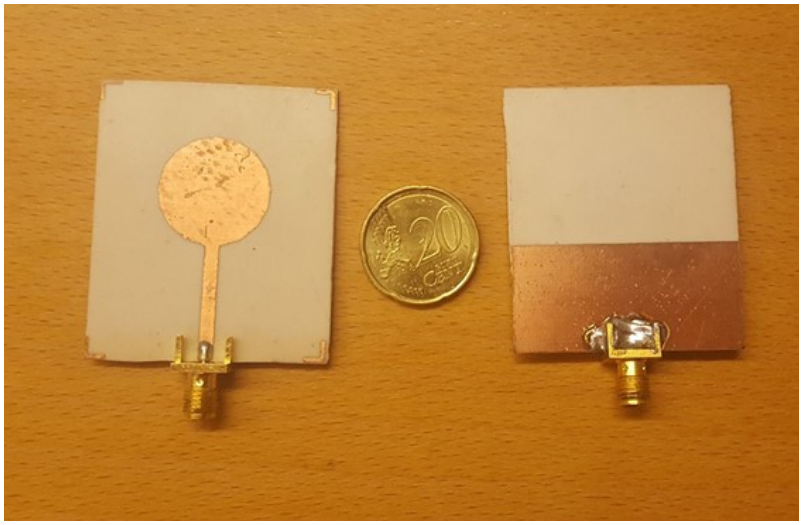

Figure 4.3: Top and bottom view of the printed disc antenna fabricated in the substrate Roger Duroid 4003C with dielectric permittivity, ε_r, 3.38 and dielectric hight, d, 0.813 mm.

4.1.3 Complete Tag System

The complete tag system corresponding to the discreet transmission line, attached to the antenna at *port-1*, through a 50 Ω SMA connector and terminated in a 50 Ω load at *port-2*, is illustrated in

Figure 4.4.

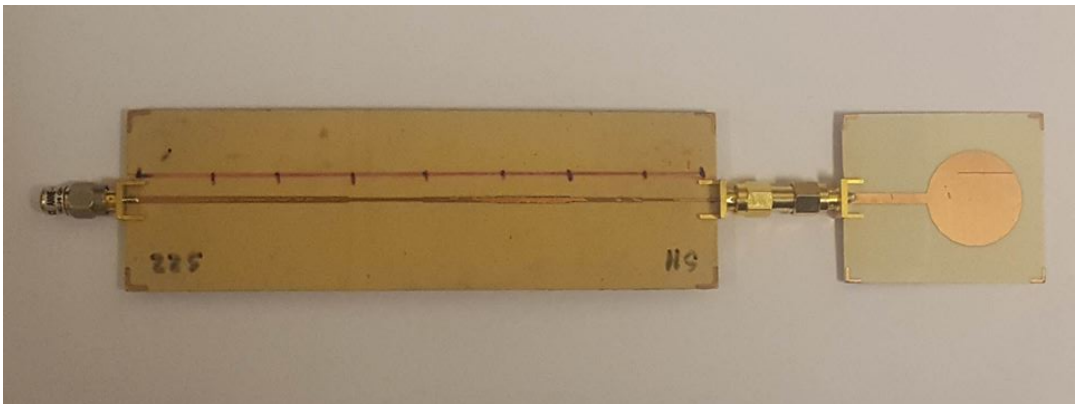

Figure 4.4: Photograph of the complete tag system.

4.1.4 Measurement Setup

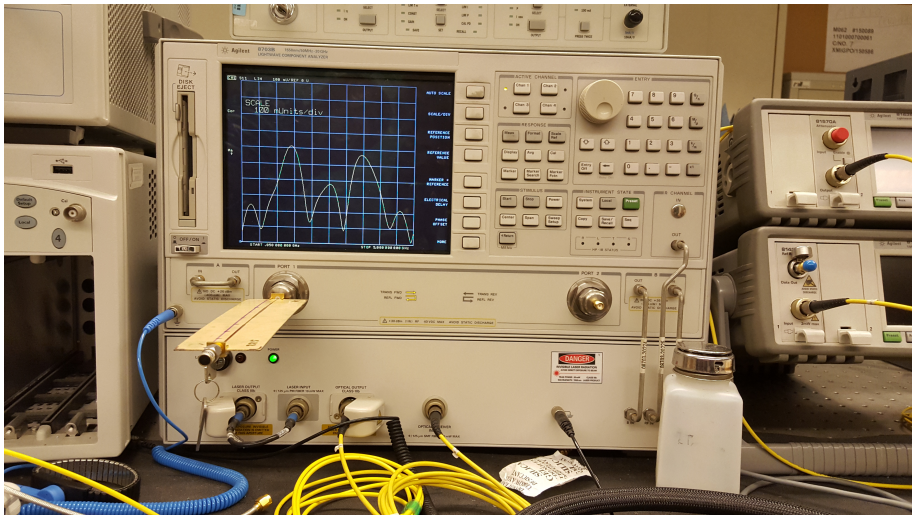

Figure 4.5: Photograph of the measurement of S_{11} reflection spectrum using a VNA.

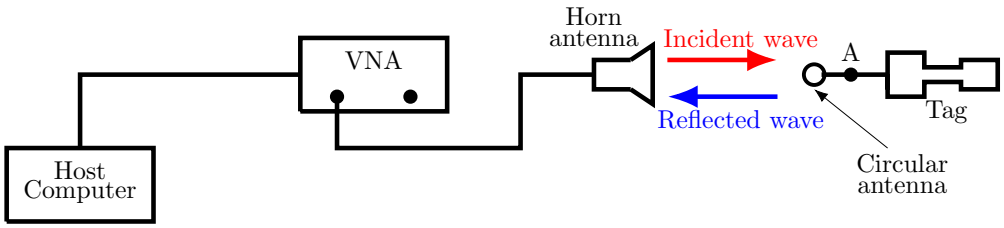

Figure 4.6: Drawing of the measurement setup.

In a first instance, the tag reflection spectrum was accessed according to the setup illustrated in Figure 4.5. To assess the tag wireless, the setup illustrated in Figure 4.6 was carried out at the

laboratory as illustrated in Figure 4.7. The transmitter/receiver functions were performed by the VNA 8703B with 5 dBm of output power.

In order to get the spectral content of the tag without considering the static error due to the cable, space propagation and mismatch effect (including the antennas), a *SOLT* (Short, Open, Load of characteristic impedance of 50 Ω) calibration was performed at the point "A" as illustrated in Figure 4.6. Next, the tag was attached at the terminal "A" and terminated in a 50 Ω load. At *port-1* of the VNA, a commercial horn antenna, illustrated in Figure 4.7, with 20 dBi gain (average) and frequency range of 2 to 18 GHz was used. Also, at the VNA a smooth window of 8% was considered in order to improve the S_{11} performance. Then, the data was accessed from a board PC in which the decoding process was performed.

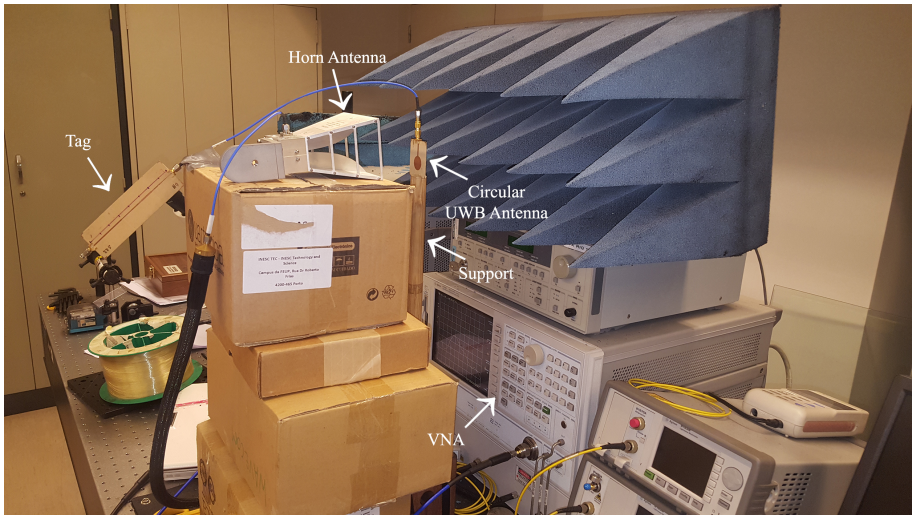

Figure 4.7: Photograph of the measurement setup.

4.2 Results

This section presents the measurement results obtained in this work. It starts by presenting the 2D Radiation Patterns. Next, the results of the tag's Reflection Spectrum are presented and discussed. After that, the performance of the DLPA is considered.

4.2.1 UWB Antennas

In this Section, the measurement results of the E-plane and H-plane 2D Radiation Patterns of the manufactured printed disc monopole antenna for two different frequencies are presented. Figures 4.8 to 4.11 depict the results measured at 4 and 6 GHz respectively. As it is possible to observe, simulation and experimental results are in good agreement. Also, it is possible to conclude that the radiation characteristics are very similar for the two considered frequencies, which means that the radiation distortions are not relevant in the frequency band of interest.

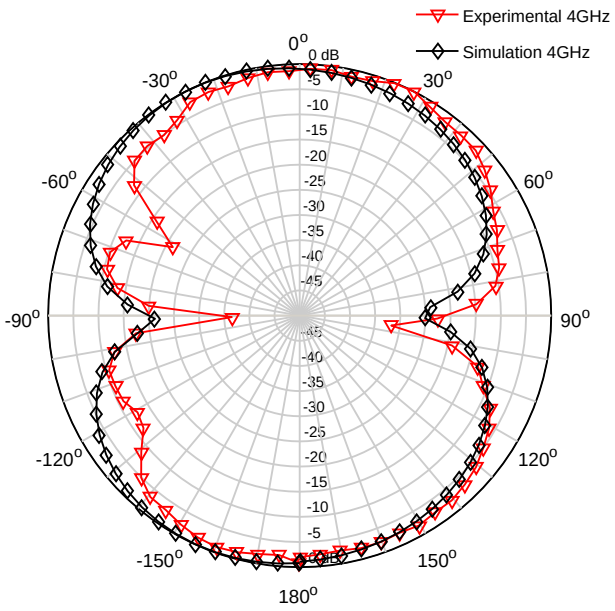

Figure 4.8: H-plane Radiation Pattern at 4 GHz.

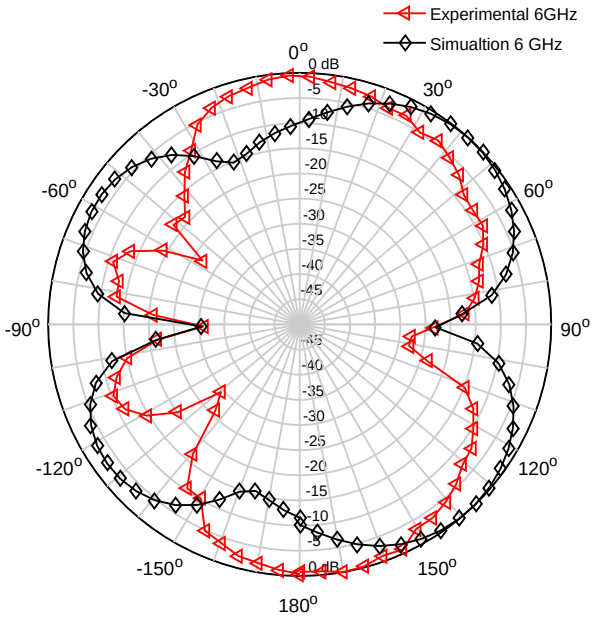

Figure 4.9: H-plane Radiation Pattern at 6 GHz.

4.2.2 Impedance Decoding by the DLPA

The assessment of the encoded impedances in a DTL is achieved following three important steps, that are: Measurement of the Reflection Spectrum, to obtain the *fitting curves* and, lastly, to apply

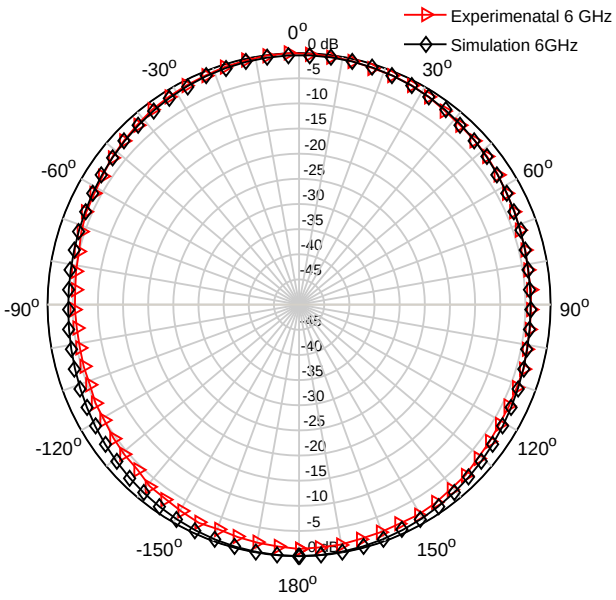

Figure 4.10: E-plane Radiation Pattern at 6 GHz.

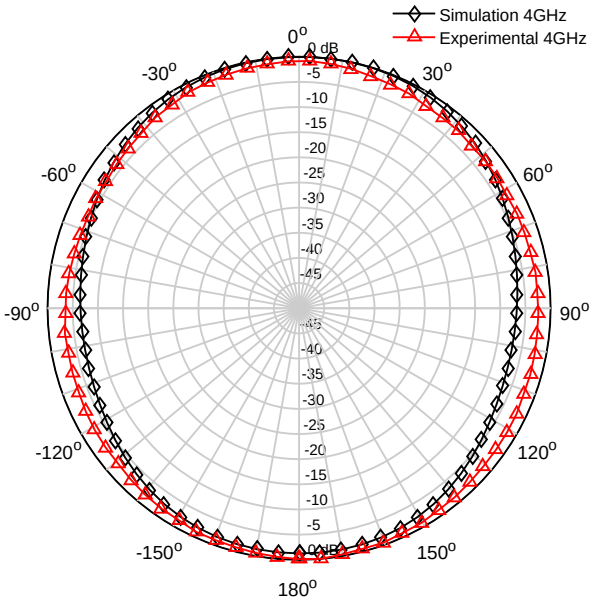

Figure 4.11: E-plane Radiation Pattern at 6 GHz.

the DLPA to the recovering of the impedances. In this Chapter, the results obtained in each of them are presented and discussed. It starts presenting the results corresponding to the the tag with 8 sections, in which the Reflection Spectrum was assessed according to the setup illustrated in

Figures 4.6 and 4.7. Next, the results corresponding to the tag with 12 sections are considered. For that, the Reflection Spectrum was measured with the tag directly attached to the VNA.

4.2.2.1 8 sections TL tag

Step-1: Reflection spectrum

Figures 4.12 and 4.13 illustrate one period of the magnitude and phase of the Reflection Spectrum respectively, of the tag composed by 8 sections TL, which is illustrated in Figure 4.2. Additionally, practical and simulation results were compared and presented as, "VNA" with square shape marker, "ADS momentum" with circle shape marker and "Theoretical" with triangle shape marker, also obtained in the electromagnetic software ADS considering ideal TL. As it is possible to conclude, simulation and measurement results are in good agreement. However, there are some differences. The observed differences, are mainly due to the substrate loss and radiation loss, as discussed in Chapter 3. Note that, the systematic errors due to the cables and mismatch effects are removed from the measurements by the VNA after correctly calibration at the frequency range of interest.

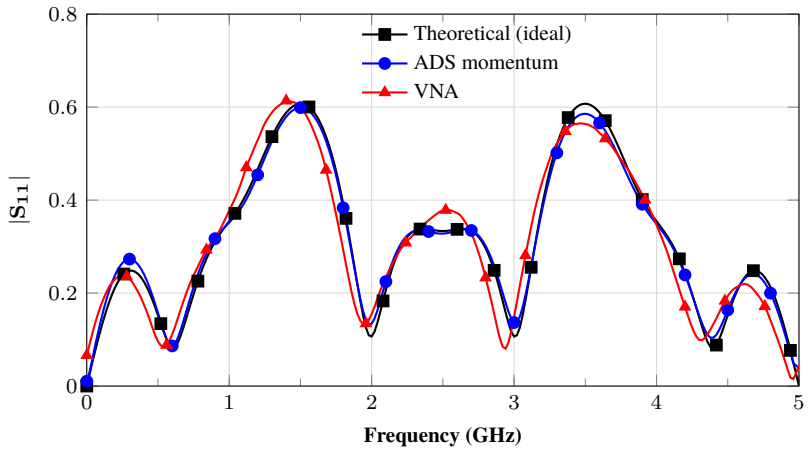

Figure 4.12: Magnitude of the reflection spectrum of tag composed by 8 sections TL depicted in Figure 4.1.

Step-2: Fitting process

After having obtained the Reflection Spectrum of the tag, the next step is to convert it from the Frequency Domain, $S_{11}(\omega)$, into the Z-Domain, $S_{11}(Z)$. This process consist in to obtain the coefficients of the numerator and denominator of the Z-Transfer Function that best fit the original spectrum in the Frequency Domain. The order of a Z-Transfer Function is defined by the number of impedance sections of the tag and its coefficients can be obtained by different methods. In this work the methods *invfreq*, *prony* and *stmcb*, where used all available in Matlab. These methods, receive the Reflection Spectrum in the Frequency Domain and the order of the desirable Z-Transfer Function and they return the coefficients of its numerator and denominator. The obtained coefficients are presented in Tables 4.4 to 4.6. Figures 4.14 and 4.15 illustrate the VNA

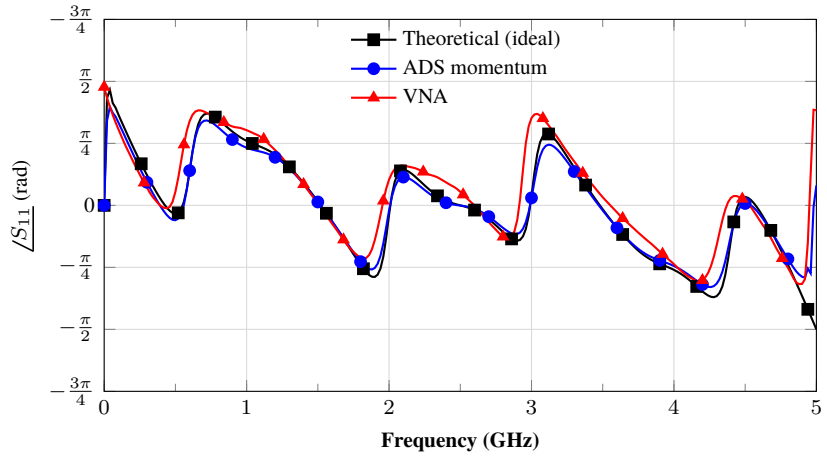

Figure 4.13: Phase of the reflection spectrum of tag composed by 8 sections TL depicted in Figure 4.1.

measurement and the fitted to the experimental data obtained with the different methods. As it is possible to see, in this specific case, all the methods produce very similar results and fitting curves were successively obtained.

Table 4.1: Coefficients of the 8*th* order reflection frequency $S_{11}(z)$ obtained with the *prony* method of the tag depicted in Figure 4.1.

Coefficients		**stmcb**	
Numerator	Denominator		
a_0	b_0	0.3187	1.0000
a_1	b_1	-0.4279	-0.5470
a_2	b_2	-0.0025	-0.2253
a_3	b_3	0.0450	-0.0452
a_4	b_4	0.2318	0.0422
a_5	b_5	0.0619	0.0432
a_6	b_6	-0.1846	-0.0112
a_7	b_7	0.0207	0.0340
a_8	b_8	0.0070	0.0003

Table 4.2: Coefficients of the 8*th* order reflection frequency $S_{11}(z)$ obtained with the *prony* method of the tag depicted in Figure 4.1.

Coefficients		**prony**	
Numerator	Denominator		
a_0	b_0	0.3176	1.0000
a_1	b_1	-0.0367	0.6798
a_2	b_2	-0.5672	-1.0183
a_3	b_3	-0.1495	-1.0102
a_4	b_4	0.3249	-0.4500
a_5	b_5	0.4921	0.0243
a_6	b_6	-0.0110	0.1391
a_7	b_7	-0.2731	0.2457
a_8	b_8	-0.0940	0.3713

Table 4.3: Coefficients of the 8*th* order reflection frequency $S_{11}(z)$ obtained with the *prony* method of the tag depicted in Figure 4.1.

Coefficients		**invfreq**	
Numerator	Denominator		
a_0	b_0	0.3176	1.0000
a_1	b_1	-0.0978	0.4876
a_2	b_2	-0.4078	-0.6695
a_3	b_3	-0.1192	-0.6831
a_4	b_4	0.2500	-0.3705
a_5	b_5	0.3856	-0.0298
a_6	b_6	-0.0171	0.0500
a_7	b_7	-0.1741	0.1249
a_8	b_8		

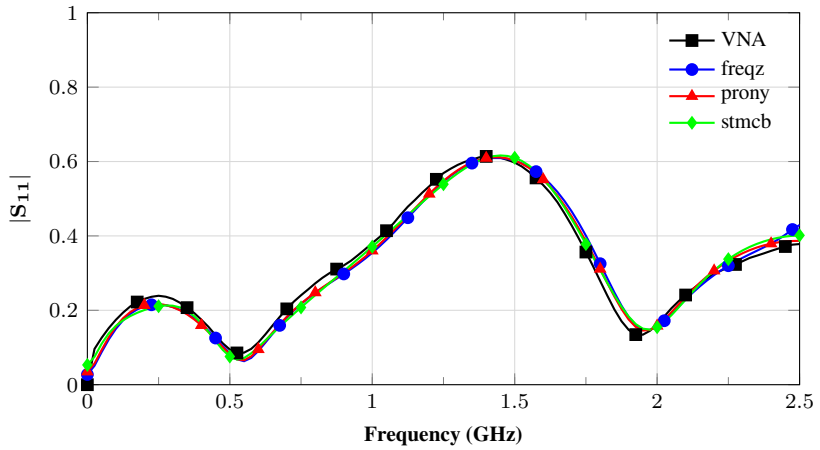

Figure 4.14: Magnitude of the measured fitting curves obtained by the different methods corresponding to the tag composed by 8 sections TL.

step-3: Results

Results for the extracted values of the impedances of the line, obtained by the DLPA are pre-

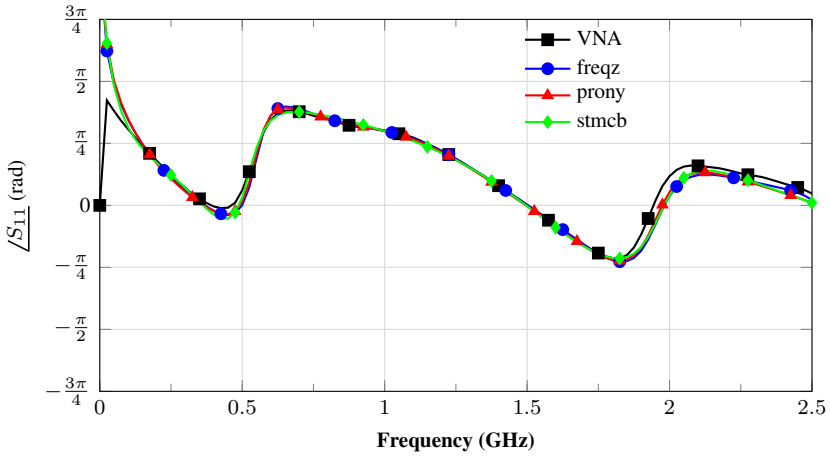

Figure 4.15: Phase of the measured fitting curves obtained by the different methods corresponding to the tag composed by 8 sections TL.

sented in Figure 4.16. Figure 4.17 corresponds to the errors magnitude obtained in each section of DTL, in which it is possible to conclude that the DLPA gives good performance in this particular case. This is due to the fact that the considered tag has only 8 sections and the impedances are in the optimal region specified in Section 3.1, which minimize the nonlinearities and distortions of the Reflection Spectrum.

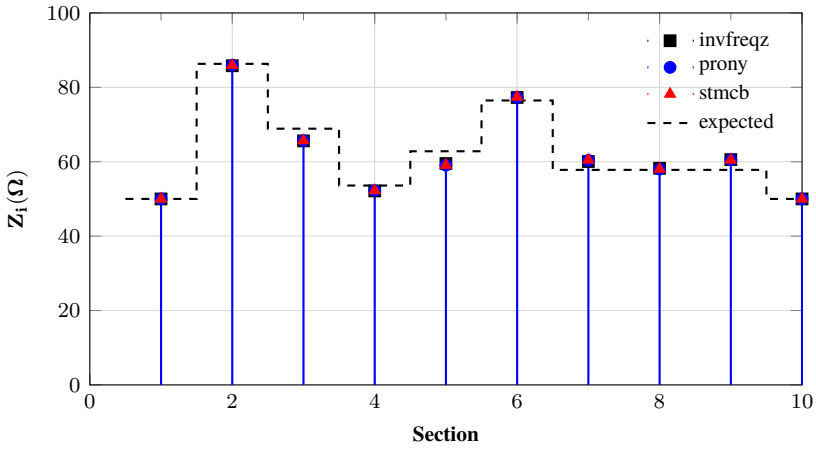

Figure 4.16: Recovered impedance of the tag composed by 8 sections depicted in Figure 4.6.

4.2.2.2 12 sections TL tag

step-1: Reflections spectrum

Figures 4.18 and 4.19 present the magnitude and phase of Reflection Spectrum of the tag composed by 12 sections TL. In Figure 4.18, comparison between simulation and measurement results are presented as, "VNA" with square shape marker, corresponding to the VNA measurement and "ADS-mom" with circle shape marker corresponding to the ADS momentum simulation. As it is

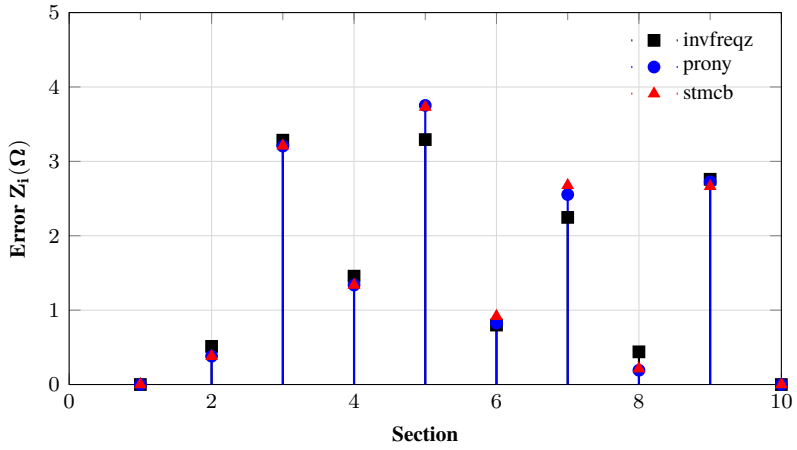

Figure 4.17: Error magnitude of the tag composed by 8 sections depicted in Figure 4.6.

possible to observe the measured result presents deviation from the simulated results, which is a critical issues to the DLPA. The mismatch between measured and theoretical results is due to the fact that the considered tag has 12 sections, which is considerably high. During this work, we have conclude that the optimal number of sections should be between 8 to 10. On the other hand, Figure 4.19 presents three curves,which are: "VNA" with square shape marker, "VNA Comp" with circle shape marker and "ADS" with triangle shape marker. The "ADS" curve corresponds to the ADS momentum simulation, and the curve labeled with "VNA" corresponds correspond to the VNA measurement, including the error introduced by the SMA connector used to attach the tag to the VNA cable. As it is possible to observe, the VNA connectors introduce a large error in the phase measurement in comparison with the ADS simulation and it is frequency dependent. In order to correct this error, it was measured the reflection spectrum of the SMA connector separated of the rest of the system and, it was verified that it has a frequency linear phase response. With this knowledge, the error was compensated introducing an opposite (negative slope) linear phase response, resulting in the curve labeled with "VNA Comp" ("VNA Comp" means compensated/adjusted measurement). Note that, similar to this, the phase depicted in Figure 4.13 was affected by the same problem, but in it the phase presented was already compensated. In terms of magnitude, the connectors have no relevant effect. Therefore, it is only necessary to remove the statical errors of the cables and the rest of the equipments, which is done by the VNA if it is systematic been properly calibrated at the frequency range of interest. For all the measurements a SOLT (Short, Open, Load of characteristic impedance of 50 Ω) calibration was considered .

Step-2: Fitting process

As it has been discussed, the first step to recover the impedance of a DTL using the DLPA is to convert the Reflection Spectrum from Frequency Domain to the Z-Domain Tables 4.4 to 4.6 present the coefficient of the Z-Transfer Function obtained using *invfreq*, *prony* and *stmcb*. The *fitting curves* obtained from them are presented in Figures 4.14 and 4.15 for magnitude and phase,

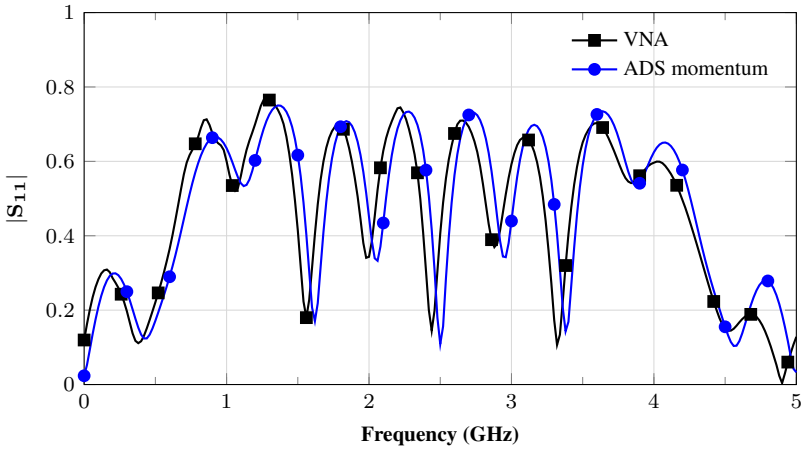

Figure 4.18: Magnitude of the reflection spectrum of tag composed by 8 sections TL depicted in Figure 4.2.

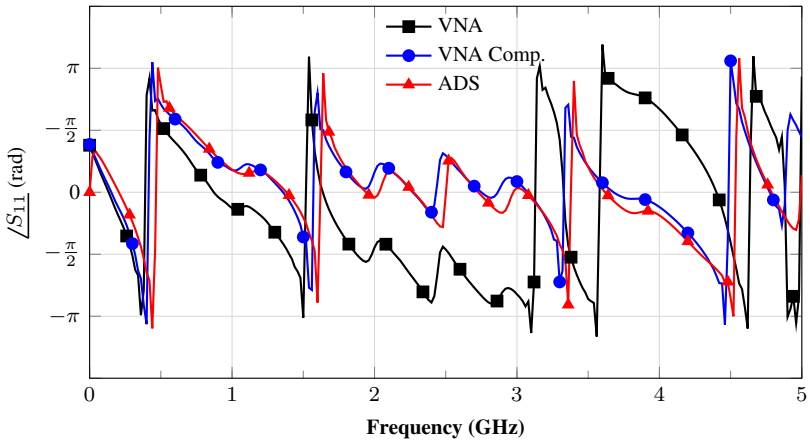

Figure 4.19: Phase of the reflection spectrum of tag composed by 8 sections TL depicted in Figure 4.2.

respectively. As it is possible to conclude, the *fitting process* present good results. However, it is remember that, the original curves that we are fitting exibit some distortion. Thus, the curves obtained from the fitting methods also are corrupted.

Step-3: Results

Figure 4.22 presents the results of the DLPA for the tag composed of 12 sections and Figure 4.23 presents the magnitude of the errors obtained in each section. As is it possible to observe, the errors obtained are greater than the tag of 8 sections. This is due to the fact that the reflection spectrum of the 12 sections has a higher distortion level and nonlinearity. Additionally, it is possible to conclude that the errors increase from section to section. This fact is explained by the recursive nature of the DLPA. As described in Chapter 2 the reflection spectrum is reconstructed at the beginning of each section, thus the errors are accumulate. Therefore, we can conclude that the performance on the DLPA in a practical scenario depend of the number of impedance sections, decreasing for increasing number sections.

Table 4.4: Coefficients of the $12th$ order reflection frequency $S_{11}(z)$ obtained with the stmcb method corresponding to the tag depicted in Figure 4.2.

Coefficients		**stmcb**	
Numerator	Denominator		
a_0	b_0	0.3187	1.0000
a_1	b_1	-0.4279	-0.5470
a_2	b_2	-0.0025	-0.2253
a_3	b_3	0.0450	-0.0452
a_4	b_4	0.2318	0.0422
a_5	b_5	0.0619	0.0432
a_6	b_6	-0.1846	-0.0112
a_7	b_7	0.0207	0.0340
a_8	b_8	0.0070	0.0003
a_9	b_9	-0.1159	-0.0525
a_{10}	b_{10}	-0.0572	-0.0845
a_{11}	b_{11}	0.2673	0.1131
a_{12}	b_{12}	-0.1928	-0.0684

Table 4.5: Coefficients of the $12th$ order reflection frequency $S_{11}(z)$ obtained with the *prony* method corresponding to the tag depicted in Figure 4.2.

Coefficients		**prony**	
Numerator	Denominator		
a_0	b_0	0.3176	1.0000
a_1	b_1	-0.0367	0.6798
a_2	b_2	-0.5672	-1.0183
a_3	b_3	-0.1495	-1.0102
a_4	b_4	0.3249	-0.4500
a_5	b_5	0.4921	0.0243
a_6	b_6	-0.0110	0.1391
a_7	b_7	-0.2731	0.2457
a_8	b_8	-0.0940	0.3713
a_9	b_9	-0.1569	0.2194
a_{10}	b_{10}	-0.2842	-0.1119
a_{11}	b_{11}	0.1380	-0.1253
a_{12}	b_{12}	0.3043	0.0154

Table 4.6: Coefficients of the 12*th* order reflection frequency $S_{11}(z)$ obtained with the *prony* method corresponding to the tag depicted in Figure 4.2.

Coefficients		**invfreq**	
Numerator	Denominator		
a_0	b_0	0.3176	1.0000
a_1	b_1	-0.0978	0.4876
a_2	b_2	-0.4078	-0.6695
a_3	b_3	-0.1192	-0.6831
a_4	b_4	0.2500	-0.3705
a_5	b_5	0.3856	-0.0298
a_6	b_6	-0.0171	0.0500
a_7	b_7	-0.1741	0.1249
a_8	b_8	-0.0575	0.2418
a_9	b_9	-0.1416	0.1579
a_{10}	b_{10}	-0.2373	-0.0714
a_{11}	b_{11}	0.1388	-0.0293
a_{12}	b_{12}	0.1379	-0.0467

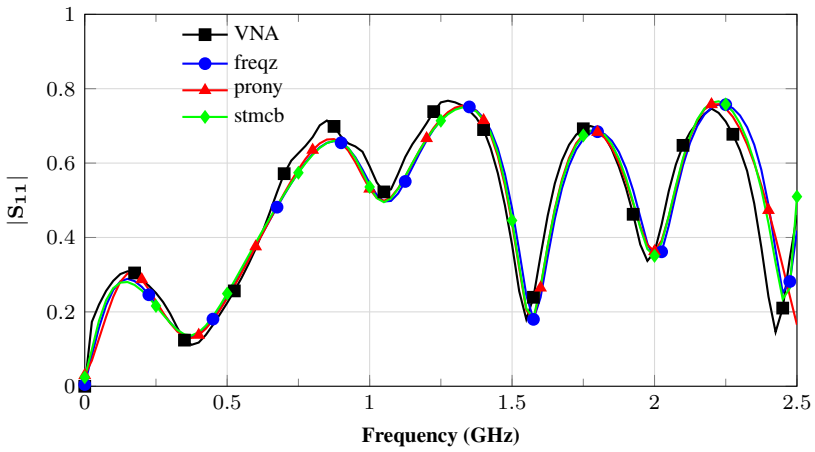

Figure 4.20

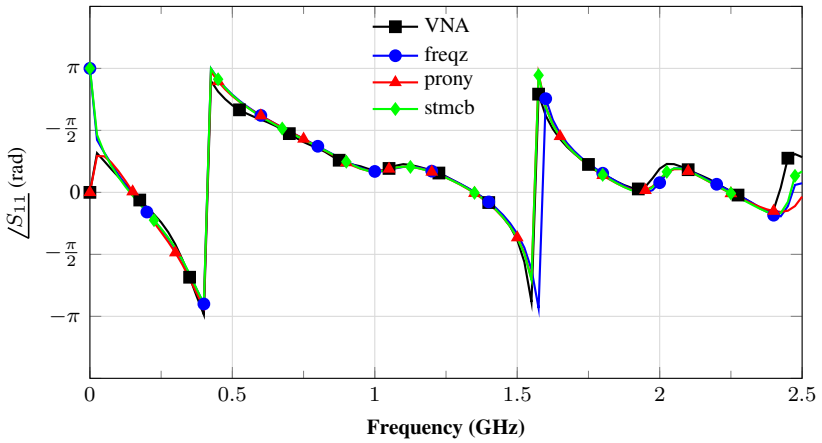

Figure 4.21

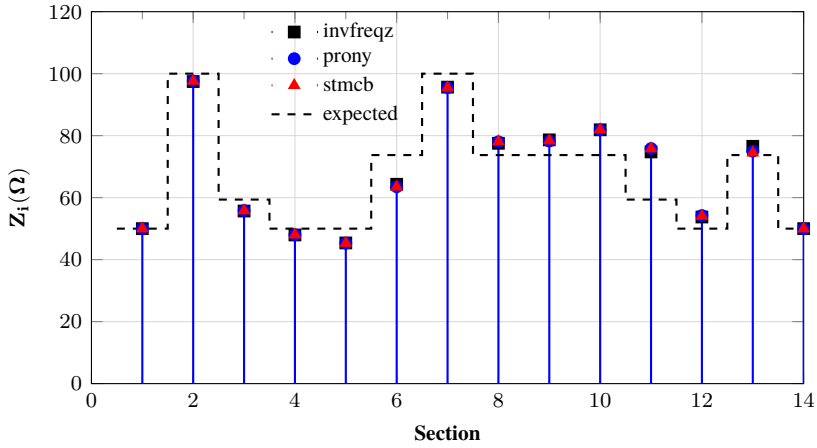

Figure 4.22: Error impedance at each section of the 12*th* section tag depicted in Figure 4.2 considering the setup illustrated in Figure 4.6.

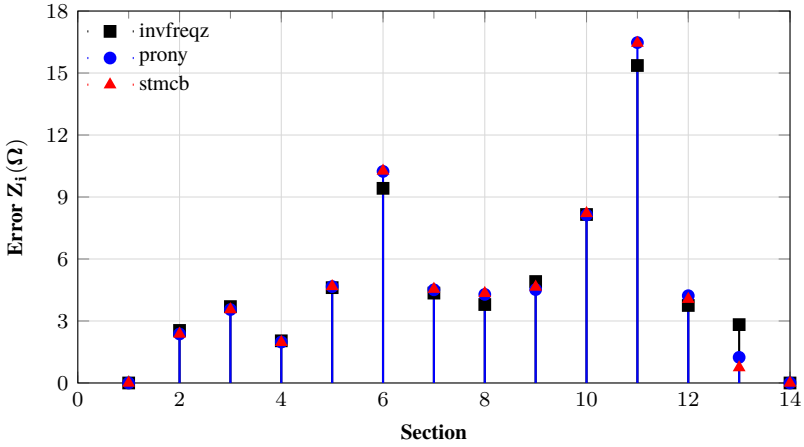

Figure 4.23: Error impedance at each section of the 12*th* section tag depicted in Figure 4.2 considering the setup illustrated in Figure 4.6.

4.3 Summary

In this chapter the experimental procedure was carried out in order to obtain the practical results, as well, the description and illustration of the main tools used in the present work.

Additionally, practical measurements obtained in this work were presented. We started with the Radiation Patterns and the S_{11} of the printed disc UWB antenna and next, the tag's measurement were presented for two different cases. After that, results of the DLP were presented and discussed. Additionally, we have concluded that, the performance of the DLPA in a practical scenario depends of the number of impedance sections. For the tag composed by 8 sections, the DLPA demonstrated a good performance. However, for the tag composed by 12 sections, the errors are to large. Therefore, we conclude that for tags with a number of sections higher than 10, are difficult to be decoded with acceptable error levels

Chapter 5

Conclusions and Future work

5.1 Conclusion

The main goal of this work was the performance characterization of the DLPA in a practical scenario, having in mind, the proposal of a new RFID passive tag system. Therefore, the present work started with an in-depth study of the DLPA, followed by its implementation in Matlab.

In order to validate the correct implementation of the algorithm, in a first instance the electromagnetic simulator ADS was used to simulate ideal Transmission Line. Next, the study of different combinations of impedance sections were carried out in order to estimate the maximum possible number of impedance sections that is possible to be encoded and decoded with acceptable errors, as well, the optimal impedance range.

After several simulations, including the UWB antenna used in this work, an experimental setup was mounted in the laboratory environment, in order to evaluate the performance and functionality of the algorithm in a practical scenario. The tags were interrogated using a VNA as a transceiver and, next, the data were accessed from a board PC, in which they were processed and the impedances were decoded.

The recovering impedance was accessed successfully in some cases, and therefore, the functionality of the DLPA in a practical scenario was successfully demonstrated. However, we believe that the system can be improved. For example by the study of the antennas and test of different configurations. Additionally, it would be interesting to use de-embedding methods to remove the systematic errors due to the cables, mismatch effects and losses. Please remember that, in order to remove these errors, we used a SOLT calibration.

5.2 Future work

- Improve the distance range between the tag and the reader antenna, for instance by improving the performance of the antenna and evaluating others De-embedding techniques.

- In order to reduce cost, it is desirable that the final tags would be designed in coplanar wave-guide (CPW) instead of Microstrip. CPW is easier to be printed in paper/plastic, thus reducing cost.
- Develop a complete RFID system, including the transceiver section, making the interrogation and reading of the tag independent of the VNA. An RFID transceivers is mainly composed by the following devices: Circulators, band pass filters, amplifiers, voltage control oscillators, analogue to digital converters, digital to analogue converter and mixers.
- Reduce the dimension of the tag by means of transmission lines operating at high frequency and analyse the performance of the DLPA considering others transmission line structures.

Appendix A

Matlab code

A.1 Calculation of the reflection spectrum

```
clc
clear
close all

Fc=[0E9:5E9:15E9]
epsilon=1; %free space
K=[2*pi*Fc.*sqrt(epsilon)/3E8];

F_start=0;
F_stop=15E9;
Numero_pontos=1000;
fp=linspace(F_start,F_stop,Numero_pontos);


Z=[50 10 30 10 20 50];
i=1;
Gama(1)=0;
Gamma_0=(Z(2)-Z(1))/(Z(2)+Z(1));
T=1/sqrt(1-Gamma_0^2)*[1 Gamma_0; Gamma_0 1];
Tt=T;
%T=1;
%K=2*pi*5E9/3E8;
l=[180*(pi/180)./K];

S21=ones(length(Fc),Numero_pontos);

```

```
for z=1:1:length(Fc)
    for n=1:1:length(fp)

        for i=1:1:length(Z)-1

            Gama(i)=(Z(i+1)-Z(i))/(Z(i+1)+Z(i));
            T=(1/(sqrt(1-Gama(i)^2)))*[ exp(j*(2*pi*fp(n)/3E8)*l(z)) Gama(i)*exp(j*(2*pi*fp(n)/3E8)*l(z));
                                        Gama(i)*exp(-j*(2*pi*fp(n)/3E8)*l(z)) exp(-j*(2*pi*fp(n)/3E8)*l(z))];
            Tt=Tt*T;
        end
        S11(z,n)=Tt(2,1)/Tt(1,1);
        %S11_com(n)=S11(n)*exp(j*2*(2*pi*fp(n)/3E8)*l);
        S21(z,n)=1/Tt(1,1);
        Tt=1;

    end

end
fh=figure('Name','dGmm');
set(fh, 'Position', [0, 0, 400, 225]);
plot(fp/1E9,abs(S11))
%plot(fp/1E9,abs(S21))
ylabel('S_{11} Magnitude','fontWeight','bold');
xlabel('Frequency (GHz)','fontWeight','bold');
grid


fh=figure('Name','dGmm');
set(fh, 'Position', [0, 0, 400, 225]);
hold on
%plot(fp/1E9,angle(S21p),'r:')
plot(fp/1E9,abs(S11),'b')
xlabel('Angle (rad)')

fh=figure('Name','dGmm');
set(fh, 'Position', [0, 0, 800, 500]);
```

```
63 Y=fp/1E9;
64 X=Fc/1E9
65 [X,Y] = meshgrid(X,Y);
66 Z = abs(S11);
67 plot3(X,Y,Z,'LineWidth',2)
68 grid on
69 xlabel('Central Frency (GHZ)','fontWeight','bold')
70 zlabel('S_{11} Magnitude','fontWeight','bold');
71 ylabel('Frequency (GHz)','fontWeight','bold');
```

Bibliography

[1] http://www.rfidjournal.com/articles/view?1338. Accessed: 2016-05-24.

[2] Sk Waseem Akram, K Shambavi, and Zachariah C Alex. Design of printed strip monopole antenna for uwb applications. In *Electronics and Communication Systems (ICECS), 2015 2nd International Conference on*, pages 823–826. IEEE, 2015.

[3] and others. Radio transmission systems with modulatable passive responder, March 1 1960. US Patent 2,927,321.

[4] José María Lopetegui Berganã. *PHOTONIC BANDGAP STRUCTURES IN MICROSTRIP TECHNOLOGY: STUDY USING THE COUPLED MODE FORMALISM AND APPLICATIONS*. PhD thesis, UNIVERSIDADE PÚBLICA DE NAVARRA, 2002.

[5] AM Bruckstein and T Kailath. Inverse scattering for discrete transmission-line models. *SIAM review*, 29(3):359–389, 1987.

[6] Petr Černỳ and Miloš Mazánek. Ultra wideband dipole antenna optimization. *Automatika: Journal for Control, Measurement, Electronics, Computing & Communications*, 47, 2006.

[7] C. Feng, W. Zhang, L. Li, L. Han, X. Chen, and R. Ma. Angle-based chipless rfid tag with high capacity and insensitivity to polarization. *IEEE Transactions on Antennas and Propagation*, 63(4):1789–1797, April 2015.

[8] Klaus Finkenzeller. Book tools. 2003.

[9] Panayiotis V Frangos and Dwight L Jaggard. A numerical solution to the zakharov-shabat inverse scattering problem. *Antennas and Propagation, IEEE Transactions on*, 39(1):74–79, 1991.

[10] Panayiotis V Frangos and Dwight L Jaggard. Analytical and numerical solution to the two-potential zakharov-shabat inverse scattering problem. *Antennas and Propagation, IEEE Transactions on*, 40(4):399–404, 1992.

[11] Izrail' Moiseevich Gel'fand and Boris Moiseevich Levitan. *On the determination of a differential equation from its spectral function*. American Mathematical Society, 1955.

[12] E. Gueguen, F. Thudor, and P. Chambelin. A low cost uwb printed dipole antenna with high performance. In *2005 IEEE International Conference on Ultra-Wideband*, pages 89–92, Sept 2005.

[13] HN Kritikos, DL Jaggard, and DB Ge. Numeric reconstruction of smooth dielectric profiles. *Proceedings of the IEEE*, 70(3):295–297, 1982.

[14] Nijas C M, Sajitha V R, Vivek R, Mohanan P, B. Paul, and Mridula S. Spectral extraction of chipless rfid tag using time domain analysis. In *2015 IEEE International Symposium on Antennas and Propagation USNC/URSI National Radio Science Meeting*, pages 169–170, July 2015.

[15] O. Necibi, S. Beldi, and A. Gharsallah. Design of a chipless rfid tag using cascaded and parallel spiral resonators at 30 ghz. In *Web Applications and Networking (WSWAN), 2015 2nd World Symposium on*, pages 1–5, March 2015.

[16] C. M. Nijas, S. Suseela, U. Deepak, P. Wahid, and P. Mohanan. Low cost chipless tag with multi-bit encoding technique. In *IEEE MTT-S International Microwave and RF Conference*, pages 1–4, Dec 2013.

[17] MR Pereira, HM Salgado, and JR Pereira. A novel layer peeling algorithm for the synthesis of microwave microstrip filters. In *2009 International Conference on Electromagnetics in Advanced Applications*, 2009.

[18] Mário Rui Silveira Pereira, Henrique Manuel de Castro Faria Salgado, and José Rocha Pereira. *Inverse scattering techniques for the synthesis of microwave structures*. PhD thesis, Universidade do Porto. Faculdade de Engenharia, 2014.

[19] Ramu Pillalamarri, Jyoti Ranjan Panda, and Rakhesh Singh Kshetrimayum. Printed uwb circular and modified circular disc monopole antennas. In *IEEE Applied Electromagnetics Conference, Kolkatta, India*, 2007.

[20] David M Pozar. *Microwave engineering*. John Wiley & Sons, 2009.

[21] S. Preradovic, I. Balbin, N. C. Karmakar, and G. F. Swiegers. Multiresonator-based chipless rfid system for low-cost item tracking. *IEEE Transactions on Microwave Theory and Techniques*, 57(5):1411–1419, May 2009.

[22] S. Preradovic and N. C. Karmakar. Design of fully printable planar chipless rfid transponder with 35-bit data capacity. In *Microwave Conference, 2009. EuMC 2009. European*, pages 013–016, Sept 2009.

[23] S. Preradovic and N. C. Karmakar. Multiresonator based chipless rfid tag and dedicated rfid reader. In *Microwave Symposium Digest (MTT), 2010 IEEE MTT-S International*, pages 1520–1523, May 2010.

[24] S. Preradovic, S. M. Roy, and N. C. Karmakar. Rfid system based on fully printable chipless tag for paper-/plastic-ltem tagging. *IEEE Antennas and Propagation Magazine*, 53(5):15–32, Oct 2011.

[25] Paul P Roberts and Graham E Town. Design of microwave filters by inverse scattering. *Microwave Theory and Techniques, IEEE Transactions on*, 43(4):739–743, 1995.

[26] S. Shrestha, M. Balachandran, M. Agarwal, V. V. Phoha, and K. Varahramyan. A chipless rfid sensor system for cyber centric monitoring applications. *IEEE Transactions on Microwave Theory and Techniques*, 57(5):1303–1309, May 2009.

[27] Johannes Skaar, Ligang Wang, and Turan Erdogan. On the synthesis of fiber bragg gratings by layer peeling. *Quantum Electronics, IEEE Journal of*, 37(2):165–173, 2001.

[28] Harry Stockman. Communication by means of reflected power. *Proceedings of the IRE*, 36(10):1196–1204, 1948.

[29] Md Razoun Siddiky Tohin. Passive rfid characterization based on radar cross section and backscatter power. 2014.

[30] A. Vena, E. Perret, and S. Tedjini. Chipless rfid tag using hybrid coding technique. *IEEE Transactions on Microwave Theory and Techniques*, 59(12):3356–3364, Dec 2011.

[31] A. Vena, E. Perret, and S. Tedjini. A fully printable chipless rfid tag with detuning correction technique. *IEEE Microwave and Wireless Components Letters*, 22(4):209–211, April 2012.

[32] A. Vena, E. Perret, and S. Tedjini. High-capacity chipless rfid tag insensitive to the polarization. *IEEE Transactions on Antennas and Propagation*, 60(10):4509–4515, Oct 2012.

[33] K Yekeh Yazdandoost and R Kohno. Design and analysis of an antenna for ultra-wideband system. In *14th IST Mobile and Wireless Communications Summit*, 2005.

[34] S. H. Zainud-Deen, M. A. Abo-Elhassan, H. A. Malhat, and K. H. Awadalla. Dual-polarized chipless rfid tag with temperature sensing capability. In *Radio Science Conference (NRSC), 2014 31st National*, pages 9–16, April 2014.

[35] S. H. Zainud-Deen, M. A. El-Hassan, H. A. Malhet, and K. H. Awadalla. Novel chipless tag with electromagnetic code. In *Antennas and Propagation (MECAP), 2012 Middle East Conference on*, pages 1–6, Dec 2012.